Scanning tunneling microscopy of Si(001)

R. J. Hamers, R. M. Tromp, and J. E. Demuth
IBM Thomas J. Watson Research Center, P.O. Box 218, Yorktown Heights, New York 10598
(Received 15 May 1986)

The atomic structure of the Si(001) surface has been examined with use of scanning tunneling microscopy (STM). The STM images reveal a dimer-type reconstruction and are inconsistent with chain and vacancy models. Both buckled and nonbuckled dimers are observed, giving rise to regions of (2×1), $c(4\times2)$, and $p(2\times2)$ symmetry. The surface has a high density of vacancy-type defects, which appear to induce or stabilize buckling of the dimers at room temperature. The STM images also reveal the atomic structure at steps and defects. At high annealing temperature the step density increases dramatically, eventually leading to faceting.

I. INTRODUCTION

The detailed atomic structure of the Si(001) surface has been the subject of many experimental and theoretical studies.[1-3] While this surface is of great technological importance, determination of its atomic structure has been greatly complicated by the presence of subsurface distortions extending as much as five atomic layers into the bulk,[4-10] as well as experimental difficulty in preparing a well-ordered surface.[5,11,12] As a result, low-energy electron diffraction (LEED) I-V studies[5,13-18] and other methods of surface structure determination[11,12,19-22] have been unusually ineffective in determining the Si(001) surface structure and have alternately supported various structural models. Likewise, theoretical energy minimization of calculations[23-30] have resulted in a number of proposed models, but none of these models accurately fits all of the experimental data and the energy difference between some models are so small that they are indistinguishable within the uncertainties of the calculations.[23]

Scanning tunneling microscopy (STM) has recently made it possible to directly probe the atomic structures of surfaces with high lateral resolution. In a preliminary report,[31] we presented the first STM images of the Si(001) surface and showed that the STM images consist of rows of oblong protrusions which we attributed to dimers. Some of these dimers were obviously buckled with respect to the surface plane while some appeared to be nonbuckled. We found that the buckled dimers give rise to small regions of local $c(4\times2)$ and $p(2\times2)$ symmetry while the local symmetry of the nonbuckled dimers is (2×1). Our topographs also showed that the surface has a relatively large number of defects.

In this paper, we present more extensive STM results and extend our analysis to achieve a better understanding of the atomic structure of Si(001). We first present a number of topographs of the Si(001) surface and compare these with various theoretical structural models using atomic-charge-superposition (ACS) calculations; these comparisons lead us to conclude that only dimer models are consistent with our images. We then show how defects and lattice strain affect the details of the structure and bonding of the Si(001) surface. Far from defects, only symmetric (nonbuckled) dimers are observed, while buckled dimers are often observed near surface defects. We show that dimer buckling is easily stabilized by vacancy-type defects and that these defects pin many of the dimers in particular buckling orientations. Our observations in defect-free areas lead us to conclude that at room temperature the time-averaged configuration for the dimers is symmetric, although the dimers may be dynamically buckling about this equilibrium configuration on a time scale which is short compared to the STM measurement time. Finally, we present, to our knowledge, the first direct observation of the microscopic faceting which occurs when Si(001) is heated in vacuum above approximately 1400 K.

II. EXPERIMENTAL PROCEDURES

Scanning tunneling microscopy, first developed by Binnig and Rohrer,[32] is a relatively simple technique. A fine metal tip which is mounted on three orthogonal piezoelectric transducers is brought extremely close (5—10 Å) to the sample under investigation so that the wave functions of the tip and sample overlap. When a bias voltage is applied between the tip and sample, electrons can tunnel through the vacuum barrier. If the tip is now scanned across the surface via two of the piezoelectric transducers (PET), the tunneling current tends to change due to variations in the overlap between the wave functions of the sample and tip. The degree of overlap can change due to topographic changes as well as changes in the local electronic structure (e.g., localized surface states). The particular wave functions contributing to the tunneling current can be selected to some extent by varying the magnitude and sign of the applied potential.

In these studies, our microscope is operated in a constant current mode. The Z PET, which is orthogonal to the surface plane, is in a feedback loop which applies a correction voltage to the Z PET in order to maintain a constant tunneling current as the tip is scanned across the surface. Since the piezo extension is proportional to the applied voltage, this correction voltage is a direct measure of the change in sample-tip separation. Then, the changes in voltage applied to the Z PET as the X and Y PET are

scanned across the surface can be presented as an image of the scanned area. The X and Y PET were calibrated from topographs of the Si(111)-(7×7) reconstruction where the distances are well known, and the Z PET was calibrated by looking at small steps on the Si(001) surface; our calibrations differ by less than 20% from the manufacturer's specifications.

The mechanical design of our microscope[33] differs significantly from the original design of Binnig and Rohrer.[32] In particular, we use a mechanical pivot operated by a rotary feedthrough to bring the sample into tunneling range instead of using a piezoelectric walker. In the tunneling position, the sample rests on a "foot" approximately 0.5 mm away from the tip; a mechanical mechanism then causes the sample to pivot about the foot. In this manner, the sample can be brought smoothly into tunneling distance. The sample can also be flipped up with the same mechanism and resistively heated. The microscope is in an ultrahigh vacuum (UHV) chamber with a base pressure of 7×10^{-11} Torr. The samples are n-type (P-doped) Si(001) with a conductivity of 0.1 Ω cm which were cut from a larger wafer. The $5\times15\times0.3$ mm^3 samples are cleaned in ethanol, mounted on a Ta support, and held by stainless steel clips which were separated from the sample by additional Si spacers cut from the same wafer. The samples were outgassed for extended periods of time at 850 K, briefly at 1175 K, and finally, flashed to 1325 K for approximately 2 min and gradually cooled down over a period of approximately 5 min. The samples were allowed to cool for three hours to reduce thermal drift. The UHV chamber has no other surface analytical tools, but samples mounted and cleaned in an identical manner in another chamber routinely exhibited sharp (2×1) LEED patterns at room temperature. At lower temperatures, streaking was observed and below approximately 200 K, sharp spots were observed in the $\frac{1}{4}$-order positions. The topographs shown here were taken on several samples cut from a single wafer, but equivalent results have been obtained on other p- and n-type Si(001) wafers.

Tips were prepared by electrochemical etching of tungsten wire in a 2-M NaOH solution. Topographs were measured with bias voltages ranging from −3.5 to −1 V applied to the sample while the tip was held at virtual ground using a low impedance current-to-voltage converter. The tunneling current was typically held at 1 nA. The scanning and data acquisition were performed using an IBM PC/XT personal computer, and the images were later transferred to an IBM 3081 computer for detailed analysis. During data acquisition, the tip is rastered across the surface and data is acquired in one scan direction only. In a typical high-resolution scan, data points are taken at points 0.30 Å apart in X and Y resulting in a 150×50 pixel (picture element) image of a 45×45 Å^2 area. Linear scanning rates are typically 40–100 Å/sec, allowing a topograph to be acquired in 5–10 min.

Thermal drifts and creep of the piezoelectric transducers during data acquisition cause the images to be somewhat distorted from their nominally square shape. The drift and creep rates can be measured, and the images shown here have been corrected for this distortion. Since the data acquisition time depends primarily on the number of pixels in an image, this correction is small for large-area scans but can be quite significant for small-area scans taken with a high point density. The correction involves slightly shifting successive rows to correct for drift in the x direction and expanding or contracting the image in the y direction to correct for drift in this direction. This correction also ensures that the ⟨110⟩ direction, which joins the centers of dimers in adjacent rows, is perpendicular to the ⟨1$\bar{1}$0⟩ direction, which joins the centers of dimers within a row.

III. RESULTS

A. STM images of atomically flat Si(001) surfaces

Figures 1–5 show typical gray-scale topgraphs of the Si(001) surface. In all gray-scale images presented here, white regions correspond to surface protru-

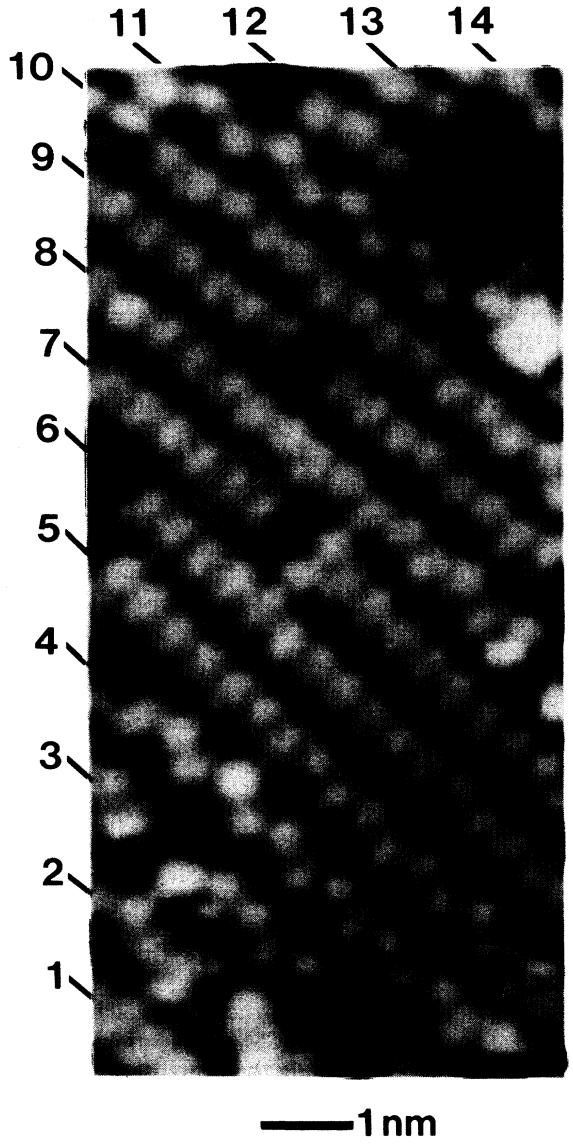

FIG. 1. STM topographs of Si(001) surface. White areas are surface protrusions and black areas are depressions, with a total gray-scale range of 1.0 Å.

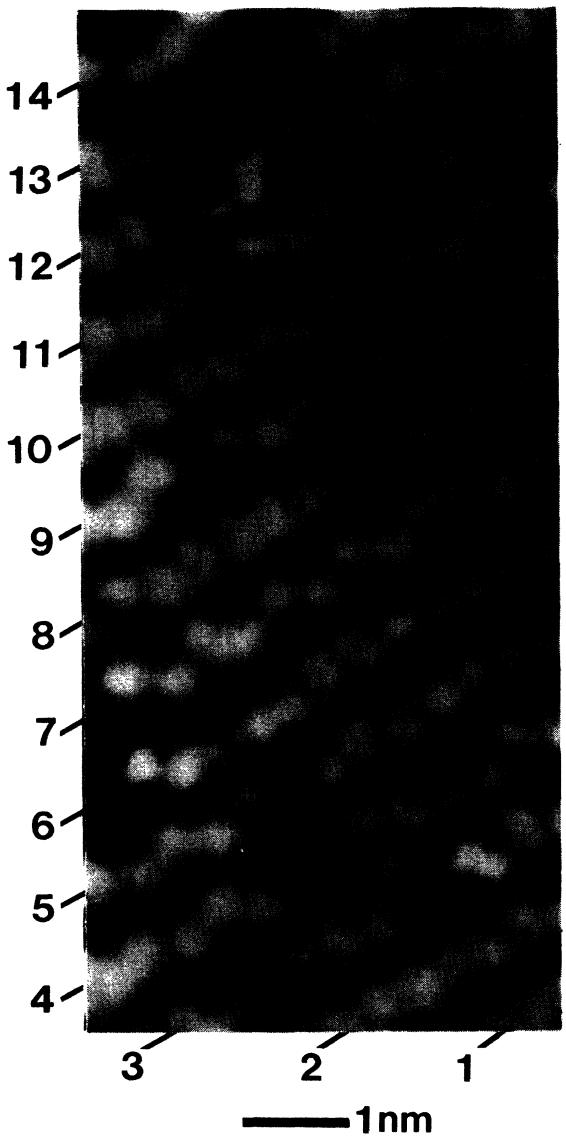

FIG. 2. Same as Fig. 1.

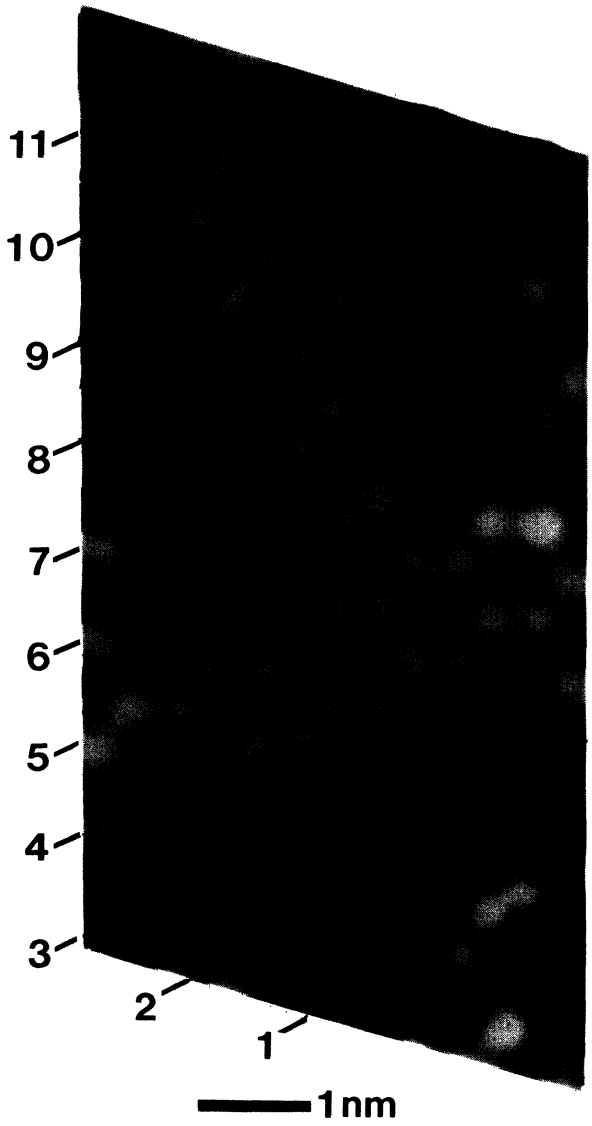

FIG. 3. Same as Fig. 1.

sions and black regions are surface depressions. Attention is drawn first to Fig. 1; in this image, the total range from white to black represents a height change of 1.0 Å. Several features of this image are immediately obvious, particularly the presence of rows of oblong protrusions, as in rows 6—10. The distance between the oblong protrusions within a row (along $\langle 1\bar{1}0\rangle$) is $a_0/\sqrt{2}$ or 3.85 Å, where a_0 is the bulk lattice constant; $a_0/\sqrt{2}$ is the lattice constant of the unreconstructed (1×1) surface. The distance between the rows (along $\langle 110\rangle$) is $a_0\sqrt{2}$, twice the lattice constant of the unreconstructed surface. Thus, the local symmetry formed by these symmetric oblong protrusions is (2×1). One (2×1) unit cell is outlined in Fig. 1. Based on such topographs, one can reasonably propose that these oblong protrusions are surface dimers. This conclusion is supported by a detailed analysis, to be presented later, which considers many alternate structural models. Another striking feature is the occasional presence of zig-zag structures, as in rows 3—5 and 11. We attribute the zig-zag structures to rows of buckled dimers in which the direction of buckling alternates from dimer to dimer along the row. In regions where we observe buckling, the direction of buckling always alternates from dimer to dimer; we do not observe structures which might be attributed to entire rows of dimers buckled in one direction. The magnitude of buckling is not always the same, as we observe varying degrees of buckling and smooth, continuous transitions between dimers which appear to be nonbuckled and those which appear to be buckled. A transition from nonbuckled to buckled dimers can be observed in row 5 of Fig. 1; in the upper left the dimers are nearly symmetric while in the lower right they are strongly buckled.

Correlation between the phase of buckling in adjacent rows of these alternating buckled dimers gives rise to $c(4\times2)$ and $p(2\times2)$ symmetries when adjacent rows are out of phase and in phase, respectively. A small $c(4\times2)$ domain can be observed in rows 3—5 of Fig. 1. Sometimes there is no clear correlation between buckling direction in adjacent rows of the buckling magnitude varies, so

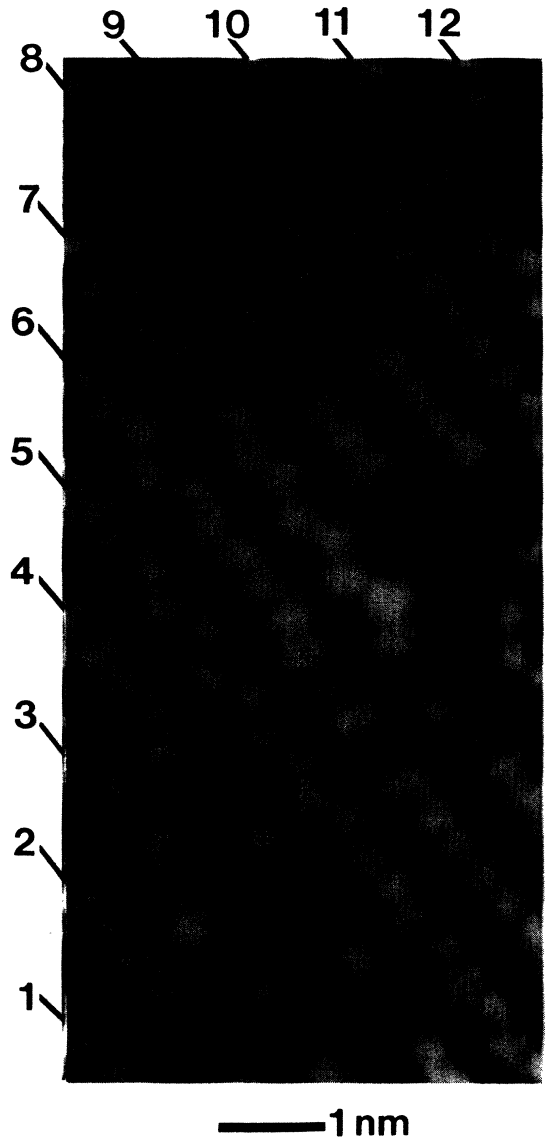

FIG. 4. Same as Fig. 1.

that the local symmetry is not well defined. An example can be found in Fig. 1, in which row 12 is defected, row 11 is buckled, and row 10 exhibits a very weak buckling which is in phase with that of row 11; since the magnitudes of the buckling in rows 10 and 11 are not equal, however, the local symmetry is not strictly $p(2\times2)$. Another important feature is the relatively high density of local surface defects. Sometimes these defects take the form of individual missing dimers, as in rows 7 and 9 of Fig. 1. Often, however, they consist of small clusters of missing dimers as in rows 3, 12, and 13. The vacancy defect in rows 12 and 13 consists of one missing dimer in each of 2 adjacent rows, but the dimers next to the vacancy appear to be pulled into the surface and toward the vacancy.

Figure 2 shows another representative area of the Si(001) surface in a relatively defect-free region. Again, both buckled (row 7, 11, and 12) and nonbuckled (rows 1, 2, 6, 8, and 9) dimers are observed. Row 10 is an excellent

FIG. 5. Large-area topograph of the Si(001) surface illustrating the high density of vacancy-type defects. The gray scale corresponds to a distance change of 1.0 Å.

example of how the buckling magnitude can vary from small or nonexistent (lower left) to very large (upper right). In rows 5—7, 9, and 10, it should be noted how the buckling is consistently largest near the missing dimer defect in each row and gradually decreases in going away from such defects.

Figure 3 shows a region of the surface which has some larger defects. In this image, the buckled dimers are much more prevalent than in the regions shown in Figs. 1 and 2. One particularly interesting feature of Fig. 3 is a transition from a $c(4\times2)$ to a $p(2\times2)$ local symmetry. One $c(4\times2)$ and one $p(2\times2)$ cell are outlined in this figure. Row 4 shows the characteristic zig-zag pattern of buckled dimers while row 5 is also zig zagged but has its phase interrupted at a missing dimer defect; thus, the local symmetry of rows 4 and 5 changes from $p(2\times2)$ at the bottom left to $c(4\times2)$ in the upper right. In the lower left corner, rows 2—4 form an extended domain of $c(4\times2)$ symmetry. Figure 4 shows more interesting structure. For example, near the center of row 6, two dimers appear to be inexplicably pulled slightly toward the bulk. Also note how in row 7 the buckling magnitude becomes very large near the vacancy defect in row 8. Adjacent to the missing dimer defect in row 10 is a pair of atoms on their bulk lattice positions; this structure may be due to silicon atoms which adsorbed atomic hydrogen, which is known to convert the (2×1) reconstruction to a (1×1). A similar effect is observed in row 7 of Fig. 1.

All these topographs demonstrate a high density of defects. The large-area topograph in Fig. 5 shows the typical size and spatial distribution of defects. The individual

dimers are not resolved in this image, but the missing dimer defects are. Virtually all of the defects consist of individual missing dimers or small clusters of 2–3 missing dimers. There is no obvious ordering of the dimers with respect to one another.

B. Evaluation of proposed Si(001) structural models

Tersoff and Hamann[34] have shown that to first order, the images obtained by constant current STM closely resemble surfaces of constant charge density. They demonstrated that for Au(110) such surfaces can easily and rather accurately be calculated by superposition of atomic charge densities. For Si(111)-(7×7) we have previously shown the utility of comparing the results of such calculations with experimental STM images, both for separating geometric from electronic effects and for comparisons with model structures.[35] While localized surface states can modify STM images, the topographs of Si(001) we present here have remained essentially the same over a range of bias voltages, although the corrugation decreases somewhat at high bias voltages. This decrease is a direct result of the increased sample-tip separation required to maintain constant tunneling current at higher bias voltages. It therefore seems reasonable to assume that these images are representative of the geometric structure of the Si(001) surface and that comparison of these images with results of ACS calculations can be used to study the surface structure in more detail. We have also recently implemented a new STM method[36] to probe the electronic structure of surfaces using the STM. Our studies of the electronic structure of the Si(001) surface[37] confirm the conclusions made here.

1. Surface structural models

Many different models of the Si(001) surface have been proposed. These models can be broadly grouped into three classes: (a) dimer models, (b) chain models, and (c) vacancy models. These will be discussed on a class by class basis, since much of the supporting and/or contradicting evidence applies to entire classes of models. Also, since there are several models belonging to each class, many of which are nearly indistinguishable with the STM, we limit our comparison to those models which we feel are most representative of each class. Figure 6 shows computer-generated ball models of some proposed Si(001) structures. These ball models assume an atomic diameter of 2.35 Å and are illuminated from above and from the side so that the topmost layers are lighter than deeper

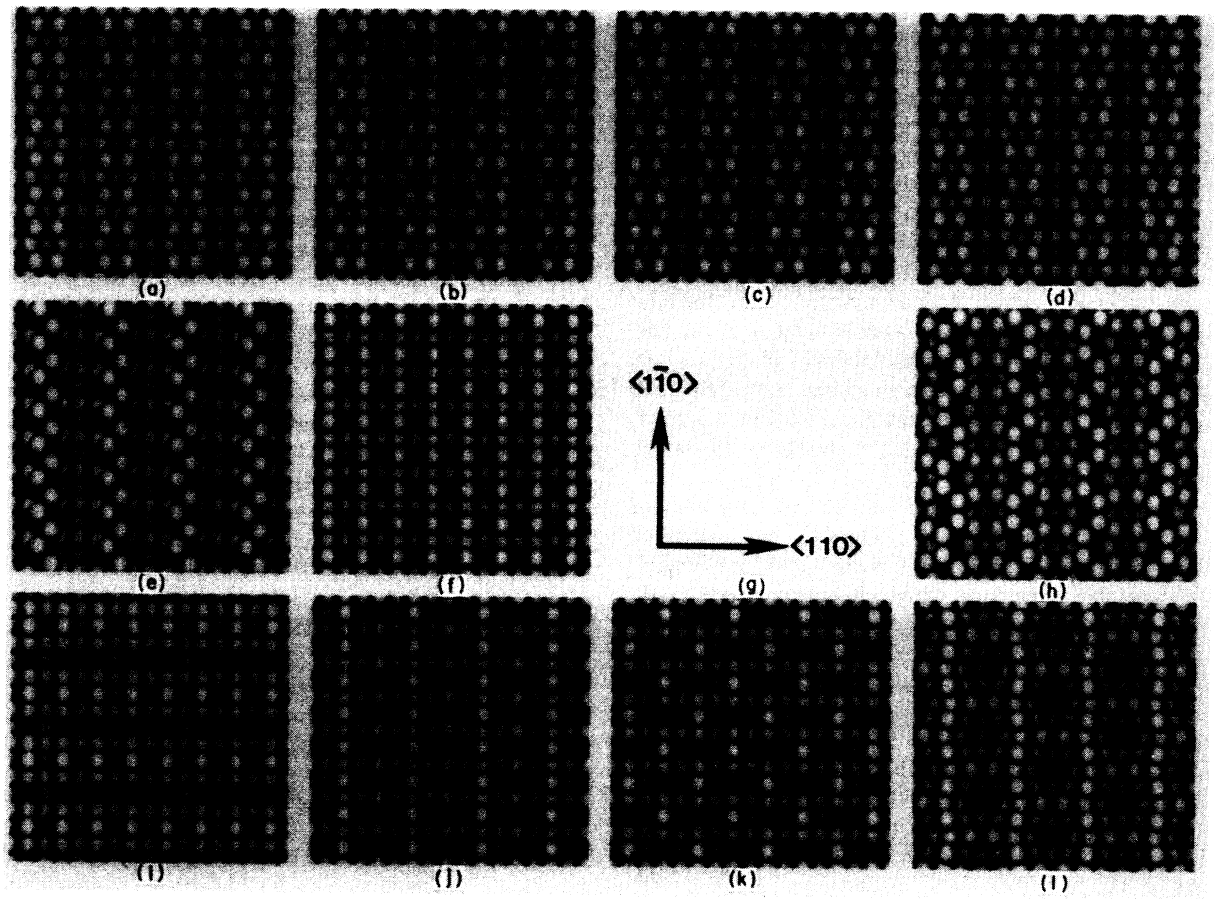

FIG. 6. Ball models of Si(001) structural models: (a) Symmetric dimer model; (b) buckled dimer models in (2×1) (c) $c(4\times2)$, and (d) $p(2\times2)$ symmetries; (e) Jona's chain model; (f) ideal (2×1) surface; (h) Northrup's dimer-plus-chain model; (i) Harrison's simple ridge, (j) symmetric ridge, and (k) $c(2\times2)$ models; (l) Poppendieck, Ngoc, and Webb's vacancy model.

layers. The ideal truncated Si(001)-(1×1) surface is shown near the center [Fig. 6(f)] while ball models for proposed theoretical structural models are shown around the border. Dimer models, chain models, and vacancy models are represented in the top, middle, and bottom rows, respectively, of Fig. 6.

(a) *Dimer models.* In their pioneering work on Si(001), Schlier and Farnsworth[38] observed a (2×1) LEED pattern. On the basis, they proposed a dimer model in which surface atoms move parallel to the $\langle 110\rangle$ direction to form symmetric dimer pairs. Dimerization lowers the total surface energy by creating an additional Si-Si bond (eliminating two dangling bonds) at the expense of increased lattice strain. Applebaum and Hamann[4] showed on the basis of a Keating strain-energy minimization calculation[39] that this surface dimerization is accompanied by substantial subsurface distortions extending 4–5 atomic layers into the bulk. Figure 6(a) shows a ball model for a strain-minimized symmetric dimer structure. Using tight-binding calculations, Chadi[24] suggested that the surface energy could be lowered further by allowing the dimers to buckle out of the surface plane. In order to minimize bond-length distortions, the buckling is accompanied by a lateral shift of the dimer which can be observed in the ball models. Chadi's (2×1) buckled dimer model, Fig. 6(b), has all dimers (both in a given row and in adjacent rows) buckled in the same direction. Alternating the direction of buckling within a row gives rise to structures with $c(4\times2)$ [Fig. 6(c)] and $p(2\times2)$ [Fig. 6(d)] symmetries which have also been detected with LEED (Refs. 5, 15, and 40) and helium scattering.[11,12] Chadi's lowest energy (2×1) structure has a buckling of approximately 0.5 Å, which corresponds to an inclination of the dimer internuclear axis of 15° with respect to the (001) plane. Other theoretical calculations[26–28] have predicted buckled dimer structures with bucklings ranging from 8° to 15°. Many other variations of dimer models have also been proposed. For example, Yang *et al.*[13,14] proposed a dimer model in which the dimer axis is twisted in the surface plane in addition to being buckled out of the surface plane, and Pandey[23] proposed a modified symmetric dimer model which incorporated defects into the structure. Such modifications of the basic dimer models will be discussed in more detail below.

(b) *Chain models.* Chain-type structural models for Si(001) were first advanced by Seiwatz,[41] and detailed models were proposed by Jona,[15] Chadi,[25] and Northrup.[29] Seiwatz suggested that conjugated chains of atoms could sit atop a dimerized Si(001) surface, but no detailed structure was proposed. Based on Seiwatz's ideas, Northrup proposed a dimer-plus-chain model, depicted in Fig. 6(h). Northrup's model can be constructed by first dimerizing the surface in the manner described by Schlier and Farnsworth and then superimposing chains of atoms in the regions between the dimerized rows. Each atom of the dimer is bonded to its dimer partner, to two atoms in the third layer, and to one chain atom; ordering of the chains produces $c(4\times2)$ and $p(2\times2)$ structures. Jona *et al.*[15] proposed a conjugated chain model for the (2×1) structure in which zig-zag chains of atoms sit atop a nondimerized Si(001) surface, and the second-layer atoms translate along $\langle 1\bar{1}0\rangle$ to minimize the elastic strain. This model is depicted in Fig. 6(e). Other modified chain models, such as Chadi's double-conjugated chain model[25] have little experimental or theoretical support.

(c) *Vacancy models.* Vacancy models have been proposed by Schlier and Farnsworth,[38] Harrison,[16] Phillips,[42] and Poppendieck, Ngoc, and Webb.[5] Harrison proposed several different vacancy models; the simplest are formed by removing every other row of the ideal Si(001) surface, producing two possible (2×1) structures. If the rows of removed atoms run along $\langle 1\bar{1}0\rangle$, then a "simple ridge" [Fig. 6(i)] is formed; if the rows of removed atoms run along $\langle 110\rangle$, then a "symmetric ridge" [Fig. 6(j)] is formed. Harrison proposed that the symmetric ridge structure would be accompanied by displacements in the second and deeper layers to form a "canted ridge" model (not shown). Vacancies could also be created in a checkerboard fashion producing a $c(2\times2)$ structure shown in Fig. 6(k). Poppendieck, Ngoc, and Webb[5] elaborated on these ideas and proposed a model which combines missing rows in the first two layers with lateral displacements in the first three layers to produce (111) microfacets, as shown in Fig. 6(l).

2. *Comparison of ACS calculations with experimental images*

We now consider surfaces of constant charge density for the theoretical structure models which were depicted in Fig. 6. We have calculated images at charge densities between 10^{-3} and 10^{-9} $e/\text{Å}^3$. As the charge density is increased from 10^{-9} to 10^{-3} $e/\text{Å}^3$, the major change is in the absolute magnitude of the corrugations, but changes also occur in the shapes of the surfaces of constant charge density which will be discussed later. We find the best overall agreement between these Si(001) results and the charge superposition calculations when a charge density of 10^{-5} $e/\text{Å}^3$ is used, as will be discussed later. This is the same charge density which, in our earlier work on Si(111)-(7×7),[35] gave quantitative agreement between the experimental images and ACS calculations for the dimer-adatom-stacking fault model of Takayanagi *et al.*[43] Here, we first present the surfaces at a charge density of 10^{-5} $e/\text{Å}^3$ to examine the qualitative, rather than quantitative features of the calculated images. We then will present a more detailed analysis which summarizes our findings for many models at many calculated charge densities.

In Fig. 7, two representative experimental images are shown in the center [7(f) and 7(g)], and the surfaces of constant charge density calculated for various structural models are shown around the perimeter [7(a)–(7e) and 7(h)–7(l)]. The identity and placement of the charge superposition images for the various model structures in Fig. 7 correspond to those of the ball models in Fig. 6. All experimental and theoretical images have been normalized to a 1 Å total gray-scale range with the same average gray value. Figure 7(f) shows a region of the Si(001) surface far away from large defects. In this case, the oval-shaped structures are nearly symmetric, although several small defects can be observed. In two locations, the oval structures are missing; the significance of such vacancy defects will be discussed later. Two undimerized atoms are also visible in the lower left corner.

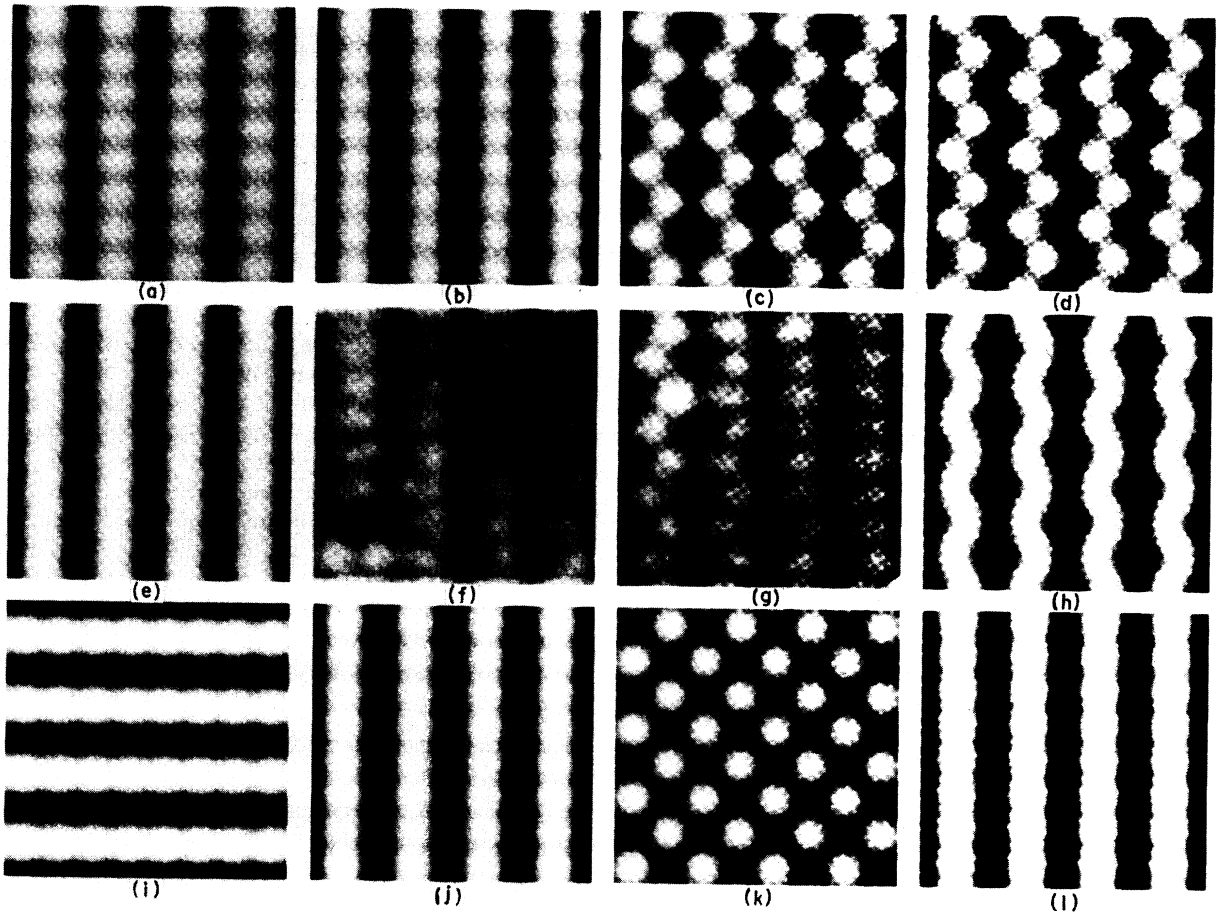

FIG. 7. Surfaces of constant charge density at 10^{-5} $e/\text{Å}^3$ for various structural models compared with experimental results: (a) Symmetric dimer model; (b) buckled dimer models in (2×1), (c) $c(4\times2)$, and (d) $p(2\times2)$ symmetries; (e) Jona's chain model; (f) experimental images from defect-free and (g) near defected regions; (h) Northrup's dimer-plus-chain model; (i) Harrison's simple ridge, (j) symmetric ridge, and (k) $c(2\times2)$ models; (l) Poppendieck, Ngoc, and Webb's vacancy model.

Figure 7(g) shows a region of the surface adjacent to a relatively large defect, which was immediately to the left of the region shown. This image shows the zig-zag structures characteristic of the surface near defects. The extended influence of surface defects is evidenced from the fact that not only the row adjacent to the vacancy shows the zig-zag structure, but the next two rows also exhibit a weak zig zag and only the rightmost row appears symmetric.

The various model structures are depicted around the perimeter of Fig. 7. In the top row, dimer models are represented by the symmetric dimer model [7(a)] and Chadi's buckled dimer model in (2×1), $c(4\times2)$, and $p(2\times2)$ symmetries in Figs. 7(b), 7(c), and 7(d), respectively. In the middle row, the experimental results are shown in the center [7(f) and 7(g)] while chain-type models are represented by Jona's model in Fig. 7(e) and by Northrup's model in Fig. 7(h). In the bottom row, vacancy models are represented by Harrison's simple ridge, symmetric ridge, and $c(2\times2)$ models in Figs. 7(i), 7(j), and 7(k), respectively, along with the model of Poppendieck *et al.* in Fig. 7(l).

Visual comparison of the experimental and calculated images shown in Fig. 7 suggests that several models appear to be in good agreement with the experimental images. The symmetric dimer model [7(a)] appears to agree best with Fig. 7(f), but Chadi's buckled dimer model [7(b)], Harrison's simple ridge and symmetric ridge vacancy models [7(i) and 7(j)], and Poppendieck's vacancy model [7(l)] all have some similarity to the experimental image of Fig. 7(f). Chadi's $c(4\times2)$ and $p(2\times2)$ buckled dimer models [7(c) and 7(d)] are very similar to the zig-zag structure observed in Fig. 7(g). The main discrepancy between the experimental results and the chain and vacancy-type models is that these models exhibit large corrugations perpendicular to the rows but only small corrugation along the rows, while our topographs show moderate corrugations along both directions. Yet, one is left to wonder whether any of a number of models could be brought into agreement with the experimental images by varying the charge density at which the theoretical images are calculated.

To address this question we have performed a detailed analysis of the corrugation profiles for the experimental results and the theoretical models at various charge densities. The detailed shapes of the corrugations can be addressed more succinctly from a Fourier analysis of the corrugations. The application of Fourier analysis to STM images has been briefly discussed by Tersoff and Hamann, but their discussion was limited to the lowest nonzero Fourier component. To describe the shape of the corrugation profiles, we must extend this discussion to higher Fourier components.

We have calculated the theoretical corrugation profiles for the various models measured along the $\langle 110 \rangle$ and $\langle 1\bar{1}0 \rangle$ axes and have Fourier analyzed these as well as our experimental data using a conventional fast Fourier transform algorithm. While this analysis could in principle be performed for both the symmetric as well as the zig-zag structures, it is attempted here only for the symmetric protrusions observed in defect-free regions of the surface because the zig-zag structures are not uniform within a given image and appear to be related to local defects. The features we shall consider in detail are the total corrugations measured on lines going through the center of the protrusions along the $\langle 110 \rangle$ and $\langle 1\bar{1}0 \rangle$ directions and the Fourier coefficients with periodicity 3.85 and 7.7 Å of the corrugation along the direction of double periodicity (which is $\langle 1\bar{1}0 \rangle$ for the symmetric ridge model and $\langle 110 \rangle$ for all others).

We first consider the magnitudes of the corrugations. Figure 8 depicts the theoretical peak-to-peak corrugations along the $\langle 110 \rangle$ and $\langle 1\bar{1}0 \rangle$ directions for various charge densities ranging from 10^{-9} to 10^{-3} $e/\text{Å}^3$ for various models. The experimental result, indicated by the rectangular box, is in excellent agreement with the symmetric dimer model, in fair agreement with the buckled dimer model of Chadi, and in disagreement with all the other models. The close spacing of the atoms along the chain in Jona's model results in a negligible corrugation along $\langle 1\bar{1}0 \rangle$, in disagreement with the experiments. Similarly, Poppendieck's model and Harrison's missing row models also predict a large corrugation when measured perpendicular to the rows but only a small corrugation along the rows. The agreement is best for the symmetric dimer model at a charge density of 10^{-5} $e/\text{Å}^3$, the same as that used in the images shown in Fig. 7.

We have also analyzed the *shapes* of the corrugation profiles along the periodicity-doubled direction using Fourier analysis. As an illustration of the application of Fourier analysis to STM images, Fig. 9 shows lines of constant charge density for the symmetric dimer model at several different charge densities; the lines pass through the center of the dimer along $\langle 110 \rangle$ direction. If the tip follows a surface of constant charge density,[34] then these lines represent the expected corrugation profiles. As the charge density is increased from 10^{-9} to 10^{-3} $e/\text{Å}^3$, the corrugation along $\langle 110 \rangle$ increases. In addition, however, there is a noticeable change in the shape of the corrugation as the individual contributions of the atoms in each dimer become more pronounced at higher charge densities. This change in shape at high charge densities manifests itself through the introduction of higher-frequency Fourier components.

Figure 10 shows the magnitude of the first (7.7 Å) and second (3.85 Å) Fourier coefficients of the corrugation along the periodicity-doubled direction as a function of charge density for various theoretical models. The experimental result (rectangular box) is in much better agree-

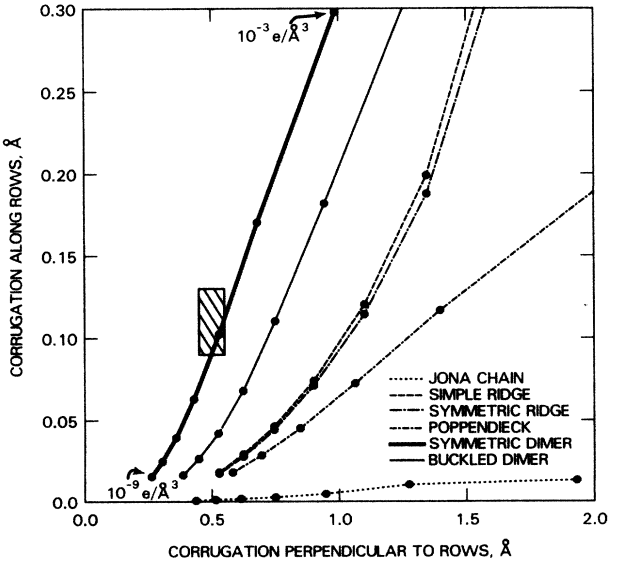

FIG. 8. Peak-to-peak corrugations along and perpendicular to rows for various structural models compared with the experimental result (box). Calculations start at 10^{-9} $e/\text{Å}^3$ nearest the origin and increase one order of magnitude at each indicated point along the lines.

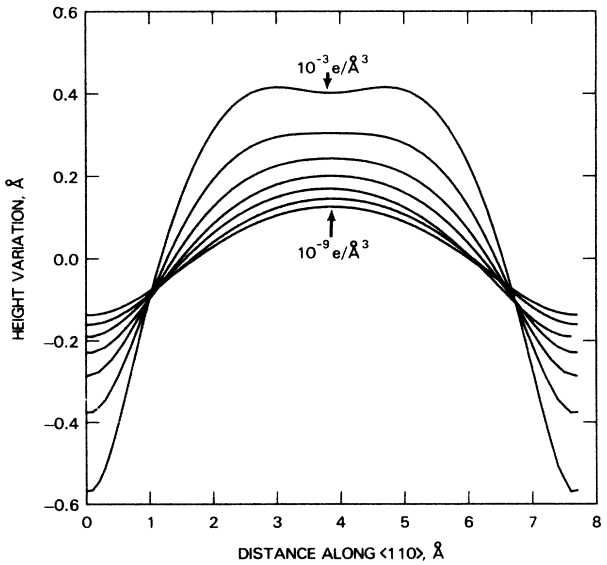

FIG. 9. Corrugation profiles along the periodicity-doubled direction ($\langle 110 \rangle$) for the symmetric dimer model at charge densities between 10^{-3} and 10^{-9} $e/\text{Å}^3$.

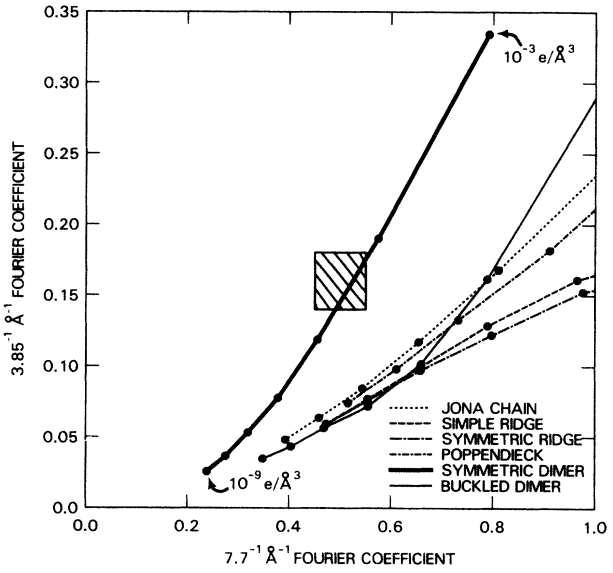

FIG. 10. Magnitude of the Fourier coefficients with periods 7.7 and 3.85 Å of the corrugation along the periodicity-doubled direction for various structural models, compared with the experimental result (box). Calculations start at 10^{-9} $e/\text{Å}^3$ nearest the origin and increase one order of magnitude at each point along the lines.

ment with the symmetric dimer model than any of the other models, and the best agreement is again achieved at a charge density of approximately 10^{-5} $e/\text{Å}^3$.

Based on the above analysis, we conclude that only dimer models are consistent with our STM images. While the symmetric dimer model is in better agreement with the experiments than the statically buckled dimer models, we have also considered a dimer which has a maximum buckling angle of 15° but which is dynamically buckling in a harmonic potential. Such a dimer spends virtually all its time near the positions of maximum buckling but when averaged over time is spatially symmetric. The charge density contours for such a time-averaged, dynamically buckling dimer are virtually indistinguishable from those of a static, symmetric dimer.

C. Defects on the Si(001) surface

1. Missing dimers

We noted earlier that our surfaces contain a relatively large number of defects; the large-area scan in Fig. 5 has a defect density of approximately 10%. Pandey[23] proposed that individual vacancy defects stabilize the Si(001) surface. When a surface dimer is removed, the two dangling bonds originally present on the removed dimer are eliminated, and one new dangling bond on each of four second-layer atoms is produced; the second-layer atoms can then translate parallel to $\langle 1\bar{1}0\rangle$ and form two second-layer dimers. In effect, this defect completely removes the two dangling bonds originally present on the surface dimer, albeit at the expense of elastic strain. As long as the strain fields of the defects do not overlap, the total surface energy should decrease. Pandey estimated that the lowest-energy structure would be formed when approximately every fourth dimer was missing, producing a defect density on the order of 25%.

While our defect density is somewhat lower than 25% and many of the defects we observe are larger than those predicted by Pandey, we do sometimes observe individual missing dimer defects, as in rows 7 and 9 of Fig. 1. The defects do not appear to be ordered; such ordering might be anticipated to result in the lowest-energy surface structure.

We noted earlier that in regions far from defects the surface appears to consist of symmetric dimers, while in defected areas we predominantly observe buckled dimers. This suggests that such defects either induce or stabilize buckling in adjacent dimers. In order to investigate the effect of vacancy defects on dimer buckling, we have performed a Keating-type strain-energy minimization[39] for Pandey's missing dimer defect. This calculation predicted that the dimers adjacent to the defect (in the same row) should be pulled slightly into the surface and toward the defect. This effect can be observed in rows 12 and 13 of Fig. 1. The experimentally observed defect also appears to induce pronounced buckling in adjacent rows (Fig. 1, rows 11 and 14) whereby the dimer atoms adjacent to the defect move away from the surface. Close examination of the STM images shows that a single defect can induce or stabilize buckling two or three atomic rows away. The Keating calculations we performed significantly underestimate the degree of buckling induced by these defects. This is probably due to the fact that the Keating calculations do not take into account changes in the electronic structure and thereby overestimate the energy cost associated with dimer buckling.

The question arises whether the high defect density is an artifact of our sample preparation procedures or is intrinsic to the Si(001) surface, as proposed by Pandey.[23] In our studies of Si(111)-(7×7),[33,35,36] we found that similar preparation conditions repeatedly gave us clean, atomically flat surfaces with a low density of defects (as judged by STM), and LEED studies showed sharp, low-background patterns. We have conducted LEED studies of Si(001) using sample holders and surface preparation procedures identical to those in our STM studies and consistently obtained sharp, low-background (2×1) LEED patterns with no evidence for higher-order reconstructions at room temperature. This demonstrates that a sharp, low-background LEED pattern does not guarantee a low density of defects and suggests that the high defect density is intrinsic to this surface, although we have not performed a detailed investigation of how surface preparation techniques affect the surface quality. However, if this defect density is typical of Si(001) samples used in other studies, the LEED I-V profiles, helium diffraction patterns, and electronic band-structure measurements should all be affected in some way by the presence of these defects.

2. Steps

Further clues to the bonding and energetics of the Si(001) surface can be obtained by examining the behavior

near steps. Just as dimer buckling is induced by vacancies, it is also induced at step edges. Figure 11 shows a topograph of a step along the $\langle 110 \rangle$ direction, with a small kink forming a step along $\langle 1\bar{1}0 \rangle$. The top image [Fig. 11(a)] shows the step as a normal gray-scale image, while the bottom image [Fig. 11(b)] uses a split gray scale to reveal the atomic structure on both the upper and lower atomic planes. Close examination shows that both upper and lower surfaces consist of symmetric or nearly symmetric dimers, except at the edge of the step along $\langle 110 \rangle$. Row 4 of Fig. 11 shows an interesting example of a transition from nonbuckled (top right) to buckled (lower left) dimers which also illustrates step-induced dimer buckling. On the right-hand side where the dimers in row 4 are surrounded by other dimers, the dimers are symmetric; on the left-hand side where the row 4 dimers form the step edge, they are clearly buckled. We have observed identical behavior on all other $\langle 110 \rangle$ step edges; while the terraces may exhibit varying degrees of buckling due to missing dimer defects, the upper step edge is always strongly buckled. Furthermore, the "up" atoms in the upper plane step edge are always aligned with the center of the dimer in the lower plane while the "down" atoms are aligned with the gap between dimer rows in the lower plane. Our Keating calculations predict a buckling at the step edge in the same direction we observe, but again significantly underestimate the magnitude of the buckling.

We have also observed steps running along $\langle 1\bar{1}0 \rangle$. This is a particularly interesting situation because there are two different configurations which can occur depending on whether the atoms forming the lower step edge also participate in dimer bonding, or whether the dimer bonding starts at the next atomic row. Figure 12 shows ball models and the results of ACS calculations at 10^{-5} $e/\text{Å}^3$ for both configurations. In Fig. 12(a), the atoms forming the lower step edge participate in dimer bonding, while in Fig. 12(b), they do not. The two configurations can be distinguished simply by measuring the distance from the center of any dimer on the lower step to the first dimer observed on the upper step. If the distance is an odd number of surface lattice constants, then the atoms forming the lower step edge participate in dimer bonding, while if the distance is an even number of surface lattice constants then the atoms forming the lower step edge do not participate in dimer bonding. Our ACS calculations predict the appearance of a gray half-row at the step edge only in the former case.

We observe both types of $\langle 1\bar{1}0 \rangle$ step edges. Figure 13 shows an image of a step along $\langle 1\bar{1}0 \rangle$ in which the lower step edge atoms participate in dimer bonding. Figure 13(a) uses a single linear gray scale, and the gray half-row predicted by the ACS calculations can be observed. In Fig. 13(b), a split gray scale is used to enhance the atomic structure of the upper and lower planes; the distance from the first full dimer row in the lower plane to the first dimers in the upper plane is $3a_0/\sqrt{2}$. Figure 13 also shows a small region of a $\langle 1\bar{1}0 \rangle$ step; note the large buckling at the top of the step edge, with the up atoms in the upper step aligned with the center of the dimer rows in the lower step, as described previously. Figure 14 shows a $\langle 1\bar{1}0 \rangle$ step in which the atoms forming the lower step edge do not participate in dimer bonding; no half-gray row is observed, and the distance from the first full lower dimer row to the first upper dimers is $2a_0/\sqrt{2}$.

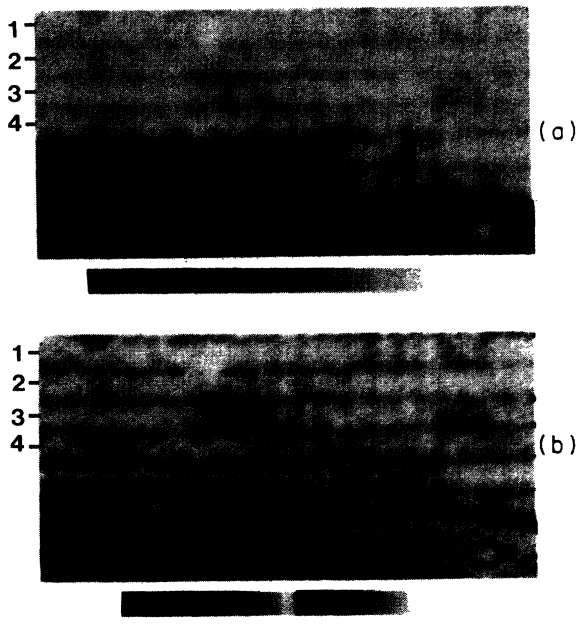

FIG. 11. Monatomic step along the $\langle 110 \rangle$ direction of the Si(001) surface. The upper image (a) uses a single linear gray scale. The lower image (b) uses a split gray scale to enhance the contrast on the terraces. Note the buckling induced at the step edge in row 4.

D. Surface roughening at high temperatures

When the Si(001) surface is heated above a critical temperature, the surface and subsurface atoms can undergo extensive reconstructions to form small (111) facets with (001) terraces. This results in a microscopic roughening of the surface which has been observed previously in reciprocal space using LEED (Ref. 44) and reflection high-energy electron diffraction (RHEED) (Ref. 45) but has now been observed in real space with the STM.

Figure 15 shows a topograph of a Si(001) surface which was annealed for 3 min at 1375 K and cooled down over 5 min. This annealing temperature is slightly higher than our typical annealing temperature of 1325 K. At temperatures slightly above 1350 K, an increased step density is observed, with a typical distance between steps of 30—40 Å. At this temperature, most of the steps are only one or two atoms high. When the surface is heated to 1450 K and cooled as above, Fig. 16 shows that only small (001) terraces remain and the surface becomes macroscopically rough.

IV. DISCUSSION

Based on the comparison of our STM images with the results of the ACS calculations, we conclude that only dimer models are consistent with our STM results. The STM images clearly show that the buckled dimers ob-

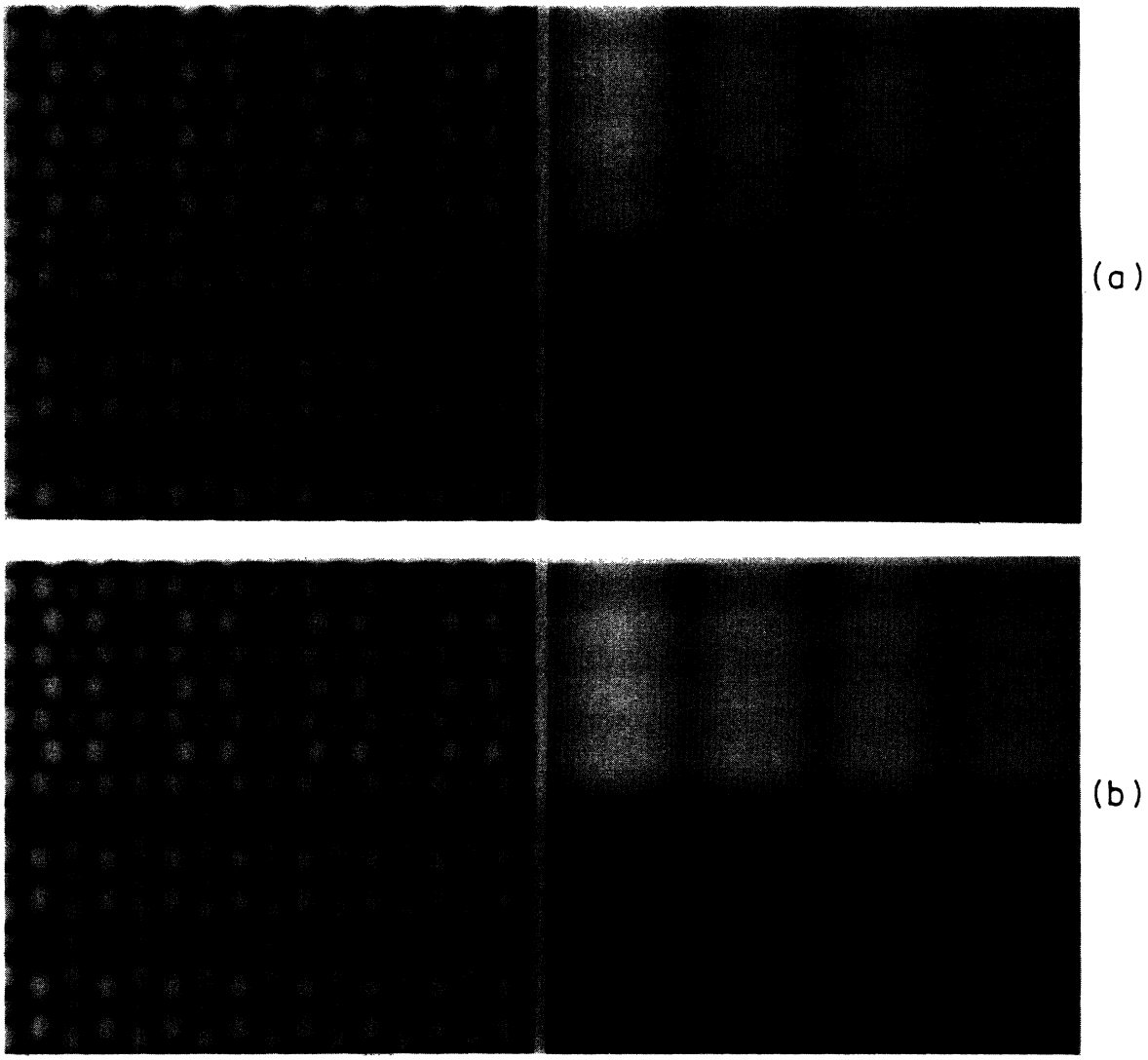

FIG. 12. Two possible atomic configurations for a step along the $\langle 1\bar{1}0 \rangle$ direction. In the top configuration (a), the atoms forming the lower step edge participate in dimer bonding, while in the lower configuration (b), they do not. Also shown are results of ACS calculations for the two configurations, which predict a gray half-row only in the former case.

served at room temperature are associated with steps and defects. While these conclusions regarding the basic dimer model are in agreement with various other experimental results, the observation of apparently symmetric dimers in defect-free regions appears to be in contradiction to previous experimental and theoretical studies which have provided evidence for dimer buckling.

For example, various ion-scattering studies[6–10] have consistently found best agreement with dimer models, and those by Tromp *et al.* find best agreement for buckled dimer models. Similarly, helium diffraction studies by Cardillo and Becker[11,12] also find best agreement with dimer models although the agreement between calculated and experimental diffraction patterns is poor except for buckled dimers in a $c(4\times2)$ structure.

LEED I-V studies, on the other hand, have been unusually indecisive about the surface structure. For example, Jona[15] found that his conjugated chain model fit his LEED I-V data better than both the symmetric dimer model of Schlier and Farnsworth[38] and the vacancy model of Phillips[42] and concluded that neither dimer models nor vacancy models could be correct. However, these early LEED studies neglected subsurface distortions, while theoretical calculations and experimental ion-scattering studies[28–31] subsequently showed that there are significant distortions extending up to five atomic layers deep. More recent LEED I-V studies[17,18] which have taken into account subsurface distortions conclude that some variation of a dimer model provides the best fit to the experimental data, and an R-factor analysis by Holland, Duke, and Paton[16] of several sets of LEED I-V data concluded that the dimers were buckled by approximately 0.36 Å.

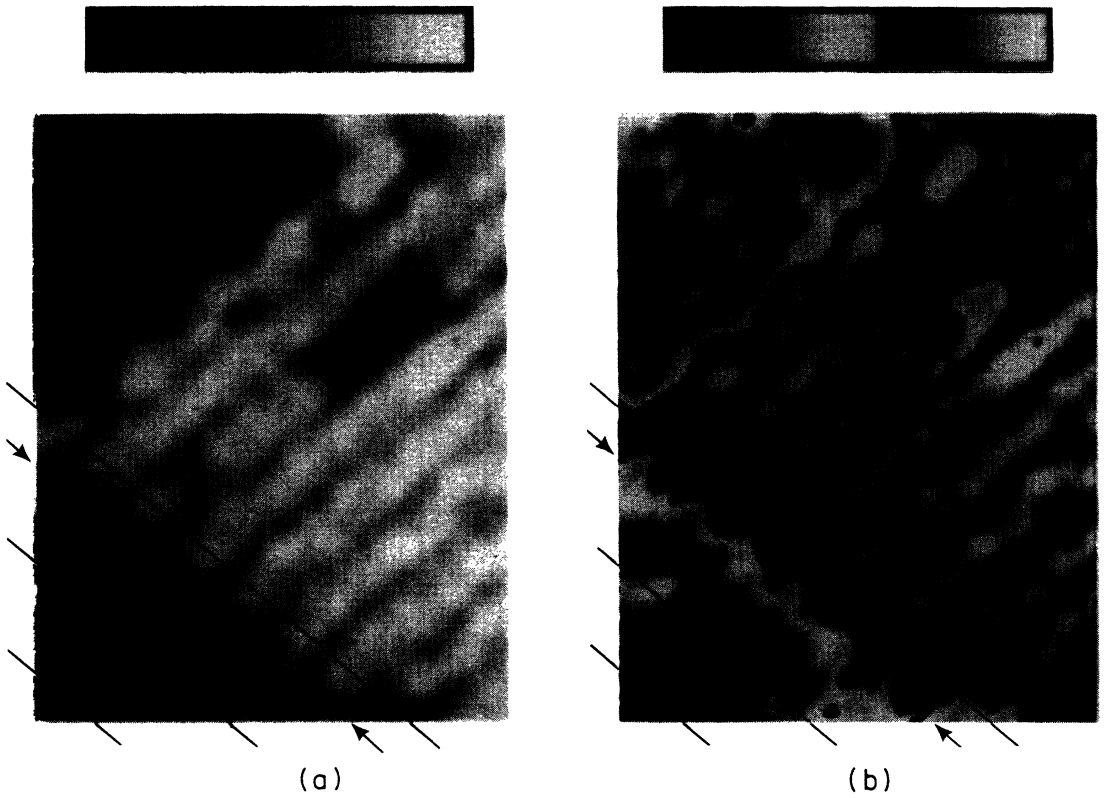

FIG. 13. Monatomic step along $\langle 1\bar{1}0 \rangle$ in which atoms forming the lower step edge participate in dimer bonding (first configuration of Fig. 12). (a) uses a single linear gray scale; the gray half-row predicted by the ACS calculations is visible. (b) are the same data imaged with a split gray scale to show the atomic spacings. Lines indicate positions of dimer rows on lower terrace and first set of dimers on upper terrace; arrows indicate position of $\langle 1\bar{1}0 \rangle$ step edge. Also note the $\langle 110 \rangle$ step edge and the large buckling at the top of this step edge, as described previously.

Yang *et al.*[13,14] have reported even better agreement between calculated and experimental LEED *I-V* data when the dimers are twisted so that the dimer axes do not lie in a $\langle 1\bar{1}0 \rangle$ plane. Yet, low-energy ion-scattering experiments by Aono[6] show a deep minimum in ion-scattering yield along $\langle 110 \rangle$ which would not be produced if the dimers were twisted. Calculations by Tromp *et al.*[10] also find dimer twisting to be energetically unfavorable, and we find no evidence for dimer twisting in our STM topographs. Thus, it can only be concluded that LEED *I-V* studies do not result in a unique structure determination on this surface.

Theoretical band-structure and energy minimization calculations also generally agree on a dimer model, but disagree about the details of the model. For example, several photoemission studies[19–22] have shown that the surface band structure is semiconducting. Appelbaum *et al.*[46] showed that all simple vacancy models result in metallic surface states, and Kerker *et al.*[26] showed using a self-consistent pseudopotential calculation that Jona's chain model also leads to metallic surface states. The semiconducting band structure has often been interpreted as supporting only a buckled dimer model, since early calculations for symmetric dimer models predicted metallic surface states,[4,46,47] while various calculations[24–28,47–51] have suggested that buckling the dimers splits the bands to produce a semiconducting band structure. However, recent cluster calculations by Redondo and Goddard[30] also predict semiconducting surface states for symmetric dimers when both electron correlation and subsurface distortions are taken into account, although cluster calculations by Verwoerd[27] predict buckled dimers. Similarly, self-consistent pseudopotential calculations by Yin and Cohen[28] predict buckled dimers, while those of Pandey[23] predict nonbuckled dimers. Pandey's calculations indicate that the energy associated with buckling is very small—less than 0.02 eV to buckle by 10°, and 0.11 eV to buckle 15°, suggesting that even the symmetric dimers may undergo a significant "dynamic" buckling at room temperature due to thermal excitation even if they are not "statically" buckled in the lowest-energy configuration.

If the lowest-energy dimer configurations is statically buckled, then at some temperature the thermal energy will overcome the barrier between the buckling directions. The presence of such order-disorder phase transitions has been predicted theoretically to occur near 230 K.[52–54] The reversible appearance of quarter-order LEED spots below a certain temperature, corresponding to a similar

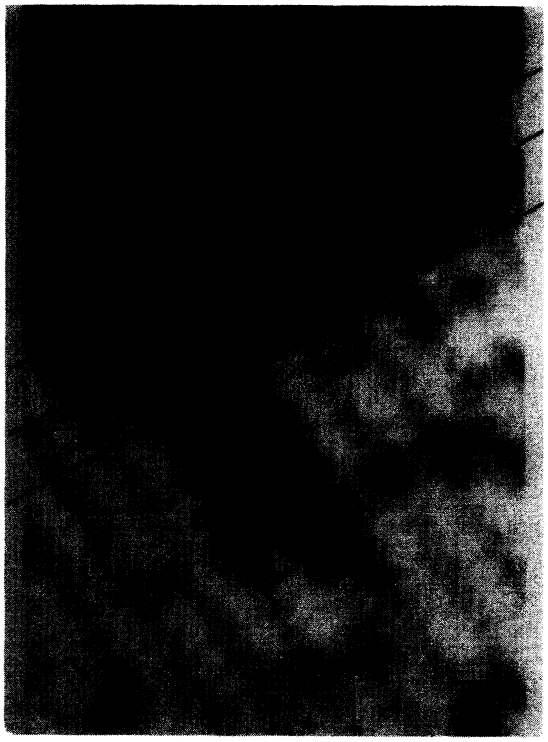

FIG. 14. Monatomic step along ⟨110⟩ in which atoms forming the lower step edge do not participate in dimer bonding (second configuration of Fig. 12).

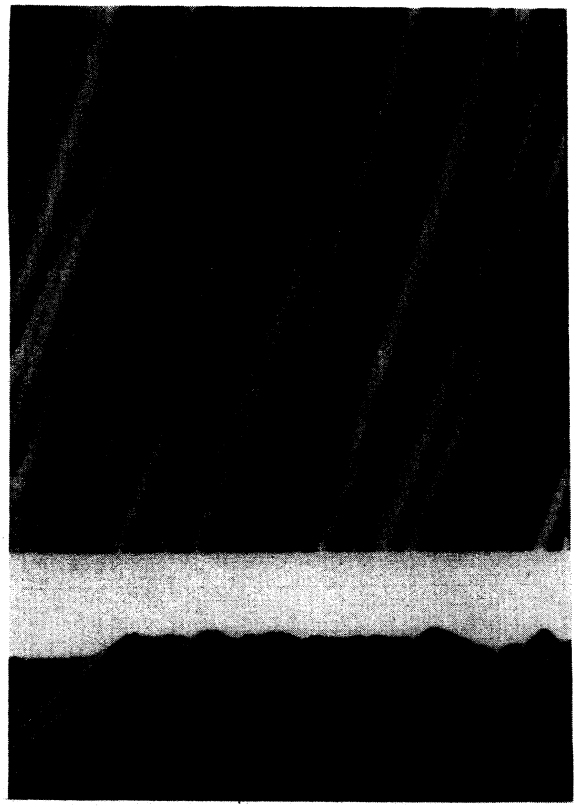

FIG. 15. 450×450 Å region of Si(001) surface which has been annealed to 1375 K and shows increased step density and initial stages of faceting. The total height variation is 14 Å. The upper image (a) is a side-illuminated topview, and the lower image (b) is a perspective view.

order-disorder transition, is known to occur on Ge(001) and has recently been observed near 230 K on Si(001).[55] We have confirmed the results on Si(001) and observe a diffuse $c(4\times2)$ pattern at 230 K and sharp $c(4\times2)$ spots at 80 K, although only a (2×1) pattern is observed at 300 K. These observations suggest that many of the dimers which appear to be symmetric in the STM images are actually rapidly buckling between the two configurations and can be "frozen" into a $c(4\times2)$ configuration at sufficiently low temperatures.

We have found from our ACS calculations that this picture of dynamically buckling dimers is consistent with our experiment results. The magnitude and shape of the corrugations expected for a time-averaged buckled dimer are virtually indistinguishable from those of a truly symmetric dimer.

The forementioned LEED observations indicate that for many dimers there is a barrier between the two buckling configurations which can be readily overcome at room temperature resulting in the time-averaged symmetric configuration which we observe in defect-free regions with STM. Yet, the LEED studies do not prove that the lowest-energy dimer configuration is buckled, as the possibility still exists that the $c(4\times2)$ structures observed in LEED at low temperatures may be associated with defects just like those observed at higher temperatures. Since the presence or absence of dimer buckling on the ideal surface is still uncertain, we cannot determine whether the dimer buckling observed at room temperature is induced or merely stabilized by defects.

The roughening we observe upon high-temperature annealing is similar to that observed in reflection high-energy diffraction (RHEED) by Norton[45] and in LEED by Gundry.[44] Gundry found that high-temperature annealing at 1475 K produced (111) microfacets which could be observed in LEED; these facets formed square etch pits as observed by scanning electron microscopy. Using RHEED, Norton found that step density greatly increased at high temperatures, and that the density of steps was higher on samples which were rapidly cooled than on those which were slowly cooled. On samples heated to 1500 K, Norton found evidence for steps along ⟨110⟩. The average step separations were 35 Å on slowly cooled (< 1 K/sec) specimens and 28 Å on quickly cooled (> 10 K/sec) specimens, close to the values we find near 1350 K. Norton also found evidence for one-dimensional disorder boundaries in which the rows of dimers shift by one surface lattice constant, $a_0/\sqrt{2}$. In our STM images, however, we have never observed a disorder boundary of this type, suggesting that the disorder detected by Norton arises from some other phenomenon.

FIG. 16. Gray-scale image of a Si(001) surface which has been annealed to 1450 K and shows faceting. The facets appear as alternating bands at 45° with respect to the axes. The total gray-scale range is 75 Å over the 1000×1000 Å area.

V. CONCLUSIONS

On the basis of our investigations, we have shown that the Si(001) surface structure consists of dimers. We observe both symmetric and buckled dimers, and we also find a high density of defects consisting of missing individual or small groups of dimers. Some of these are similar to the "missing dimer defect" proposed by Pandey, although we often observe defects consisting of two or three adjacent dimers missing in a single row rather than single missing dimers. These vacancy-type defects and steps induce or stabilize dimer buckling and are responsible for the regions of $c(4\times2)$ and $p(2\times2)$ symmetry observed at room temperature; in defect-free regions symmetric dimers are predominantly observed. The STM images represent the time-averaged configuration of the dimers; in defect-free regions these are either symmetric or are dynamically buckling on a time scale which is short compared to the STM measurement time.

We have also studied the atomic structure of monatomic steps along the $\langle 110\rangle$ and $\langle 1\bar{1}0\rangle$ directions. For steps along $\langle 110\rangle$, we find that the row of dimers forming the upper step edge are strongly buckled. For steps along $\langle 1\bar{1}0\rangle$ where two different step configurations are possi-

ble, both are observed. The buckling near steps and defects is in qualitative agreement with the results of Keating elastic strain energy minimization calculations, but the calculations significantly underestimate the degree of buckling. Finally, we have observed the formation of (111) microfacets upon high-temperature annealing of the Si(001) surface, leading to an irreversible roughening of the surface.

ACKNOWLEDGMENTS

The authors would like to acknowledge Peter Schroer, Ronald Imbihl, and Bill Thompson for experimental assistance, Richard Voss for assistance in processing images of rough surfaces, and Kosal Pandey and Jerry Tersoff for stimulating discussions. This work was supported in part by the U.S. Office of Naval Research.

[1]D. E. Eastman, J. Vac. Sci. Technol. **17**, 492 (1980).
[2]D. Haneman, Adv. Phys. **31**, 165 (1982).
[3]W. Monch, Surf. Sci. **86**, 672 (1979).
[4]J. A. Appelbaum and D. R. Hamann, Surf. Sci. **74**, 21 (1978).
[5]T. D. Poppendieck, T. C. Ngoc, and M. B. Webb, Surf. Sci. **75**, 287 (1978).
[6]M. Aono, Y. Hou, C. Oshima, and Y. Ishizawa, Phys. Rev. Lett. **49**, 567 (1982).
[7]L. C. Feldman, P. J. Silverman, and I. Stensgaard, Nucl. Instrum. Methods **168**, 589 (1980).
[8]I. Stensgaard, L. C. Feldman, and P. J. Silverman, Surf. Sci. **102**, 1 (1981).
[9]R. M. Tromp, R. G. Smeenk, and F. W. Saris, Phys. Rev. Lett. **46**, 9392 (1981).
[10]R. M. Tromp, R. G. Smeenk, F. W. Saris, and D. J. Chadi, Surf. Sci. **133**, 137 (1983).
[11]M. J. Cardillo and G. E. Becker, Phys. Rev. Lett. **40**, 1148 (1978).
[12]M. J. Cardillo and G. E. Becker, Phys. Rev. B **21**, 1497 (1980).
[13]W. S. Yang, F. Jona, and P. M. Marcus, Solid State Commun. **43**, 847 (1982).
[14]W. S. Yang, F. Jona, and P. M. Marcus, Phys. Rev. B **28**, 2049 (1983).
[15]F. Jona, H. D. Shih, A. Ignatiev, D. W. Jepsen, and P. M. Marcus, J. Phys. C **10**, L67 (1977).
[16]B. W. Holland, C. B. Duke, and A. Paton, Surf. Sci. **140**, L269 (1984).
[17]S. Y. Tong and A. L. Maldonado, Surf. Sci. **78**, 459 (1978).
[18]S. J. White, D. C. Frost, and K. A. R. Mitchell, Solid State Commun. **42**, 763 (1982).
[19]F. J. Himpsel and D. E. Eastman, J. Vac. Sci. Technol. **16**, 1297 (1979).
[20]R. I. G. Uhrberg, G. V. Hansson, J. M. Nicholls, and S. A. Flodstrom, Phys. Rev. B **24**, 4684 (1981).
[21]J. E. Rowe and H. Ibach, Phys. Rev. Lett. **32**, 421 (1974).
[22]H. A. Van Hoof and M. J. Van der Wiel, Appl. Surf. Sci. **6**, 444 (1980).
[23]K. Pandey, in *Proceedings of the Seventeenth International Conference on the Physics of Semiconductors,* edited by D. J. Chadi and W. A. Harrison (Springer-Verlag, New York, 1985), p. 55.
[24]D. J. Chadi, Phys. Rev. Lett. **43**, 43 (1979).
[25]D. J. Chadi, J. Vac. Sci. Technol. **16**, 1290 (1979).
[26]G. P. Kerker, S. G. Louie, and M. L. Cohen, Phys. Rev. B **17**, 706 (1978).
[27]W. S. Verwoerd, Surf. Sci. **103**, 404 (1981).
[28]M. T. Yin and M. L. Cohen, Phys. Rev. B **24**, 2303 (1981).
[29]J. E. Northrup, Phys. Rev. Lett. **54**, 815 (1985).
[30]A. Redondo and W. A. Goddard, III, J. Vac. Sci. Technol. **21**, 344 (1982).
[31]R. M. Tromp, R. J. Hamers, and J. E. Demuth, Phys. Rev. Lett. **55**, 1303 (1985).
[32]G. Binnig and H. Rohrer, Helv. Phys. Acta **55**, 726 (1982).
[33]J. E. Demuth, R. J. Hamers, R. M. Tromp, and M. E. Welland, IBM J. Res. Dev. **30**, 396 (1986).
[34]J. Tersoff and D. R. Hamann, Phys. Rev. B **31**, 805 (1985).
[35]R. J. Tromp, R. J. Hamers, and J. E. Demuth Phys. Rev. B **34**, 1388 (1986).
[36]R. J. Hamers, R. M. Tromp, and J. E. Demuth, Phys. Rev. Lett. **56**, 1972 (1986).
[37]R. M. Tromp, R. J. Hamers, and J. E. Demuth (unpublished).
[38]R. E. Schlier and H. E. Farnsworth, J. Chem. Phys. **30**, 917 (1959).
[39]P. N. Keating, Phys. Rev. **145**, 637 (1966).
[40]J. J. Lander and J. Morrison, J. Chem. Phys. **37**, 729 (1962).
[41]R. Seiwatz, Surf. Sci. **2**, 473 (1964).
[42]J. C. Phillips, Surf. Sci. **40**, 459 (1973).
[43]K. Takayanagi, Y. Tanishiro, M. Takahashi, and S. Takahashi, J. Vac. Sci. Technol. A **3**, 1502 (1985).
[44]P. M. Gundry, R. Holton, and V. Leverett, Surf. Sci. **43**, 647 (1974).
[45]N. G. Norton, Vacuum **33**, 621 (1983).
[46]J. A. Appelbaum, G. A. Baraff, and D. R. Hamann, Phys. Rev. Lett. **35**, 729 (1975).
[47]J. A. Appelbaum, G. A. Baraff, and D. R. Hamann, Phys. Rev. B **14**, 588 (1976).
[48]J. Pollman, A. Mazur, and M. Schmeits, Physica **117B**, 771 (1983).
[49]J. Ihm, M. L. Cohen, and D. J. Chadi, Phys. Rev. B **21**, 4592 (1980).
[50]M. A. Bowen, J. D. Dow, and R. E. Allen, Phys. Rev. B **26**, 7083 (1982).
[51]A. Mazur and J. Pollman, Phys. Rev. B **26**, 7086 (1982).
[52]A. Saxena, E. T. Gawlinski, and J. D. Gunton (unpublished).
[53]J. Ihm, D. H. Lee, J. D. Joannopoulos, and A. N. Berker, J. Vac. Sci. Technol. B **1**, 705 (1983).
[54]J. Ihm, D. H. Lee, J. D. Joannopoulos, and J. J. Xiong, Phys. Rev. Lett. **51**, 1872 (1983).
[55]T. Tabata, T. Aruga, and Y. Murata (unpublished).

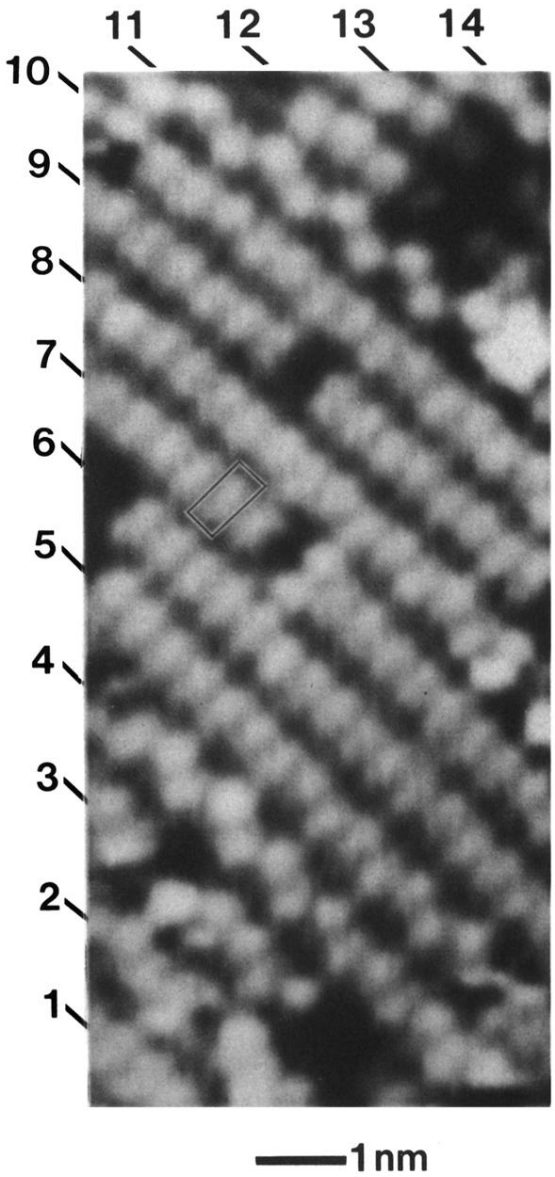

FIG. 1. STM topographs of Si(001) surface. White areas are surface protrusions and black areas are depressions, with a total gray-scale range of 1.0 Å.

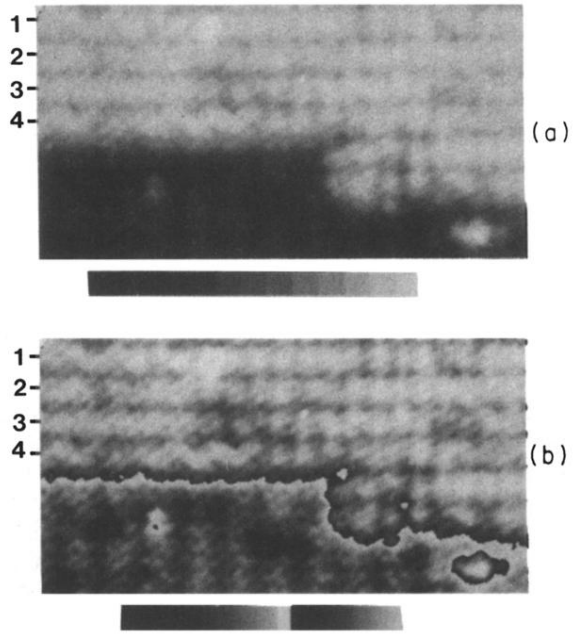

FIG. 11. Monatomic step along the ⟨110⟩ direction of the Si(001) surface. The upper image (a) uses a single linear gray scale. The lower image (b) uses a split gray scale to enhance the contrast on the terraces. Note the buckling induced at the step edge in row 4.

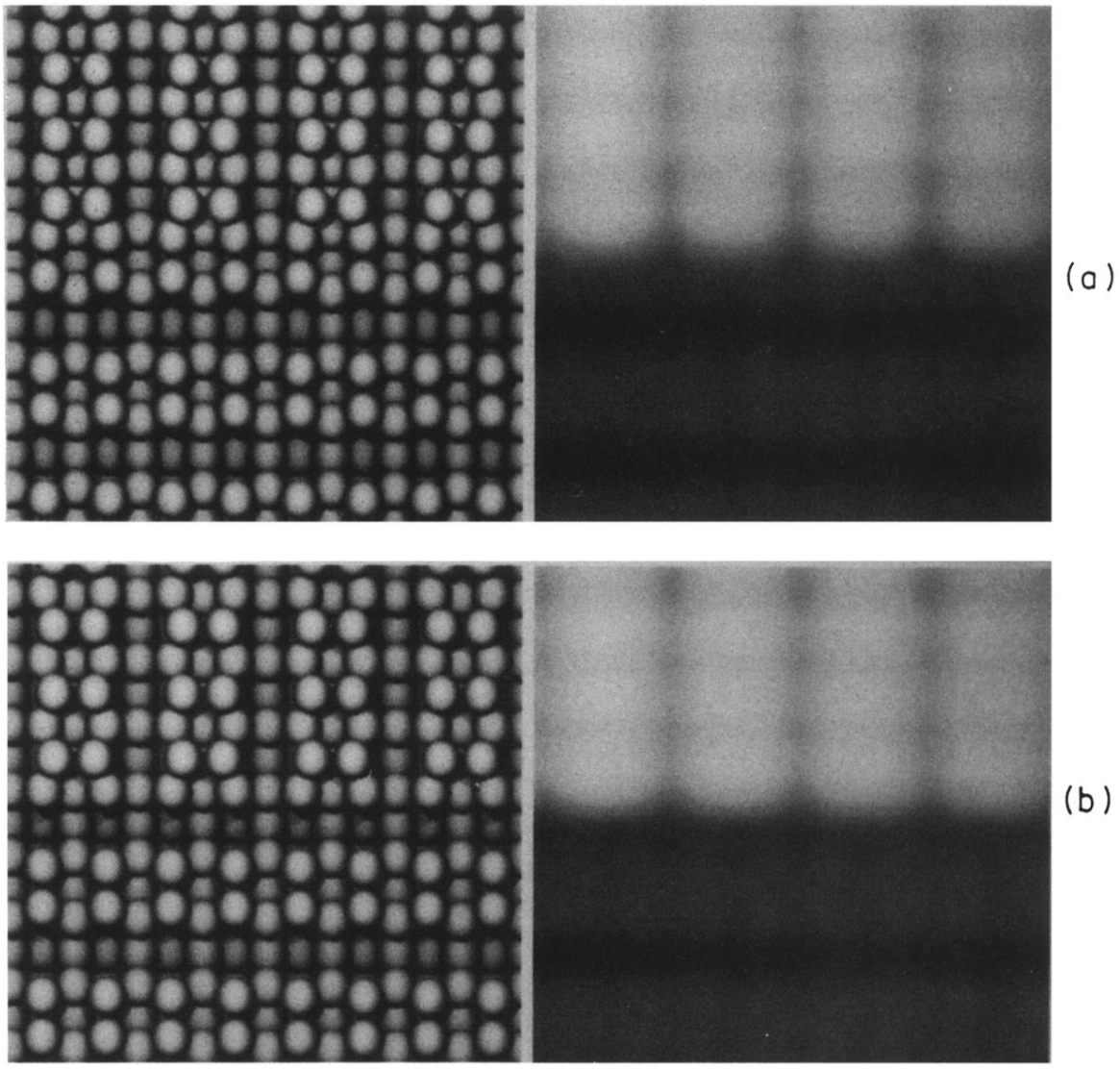

FIG. 12. Two possible atomic configurations for a step along the $\langle 1\bar{1}0 \rangle$ direction. In the top configuration (a), the atoms forming the lower step edge participate in dimer bonding, while in the lower configuration (b), they do not. Also shown are results of ACS calculations for the two configurations, which predict a gray half-row only in the former case.

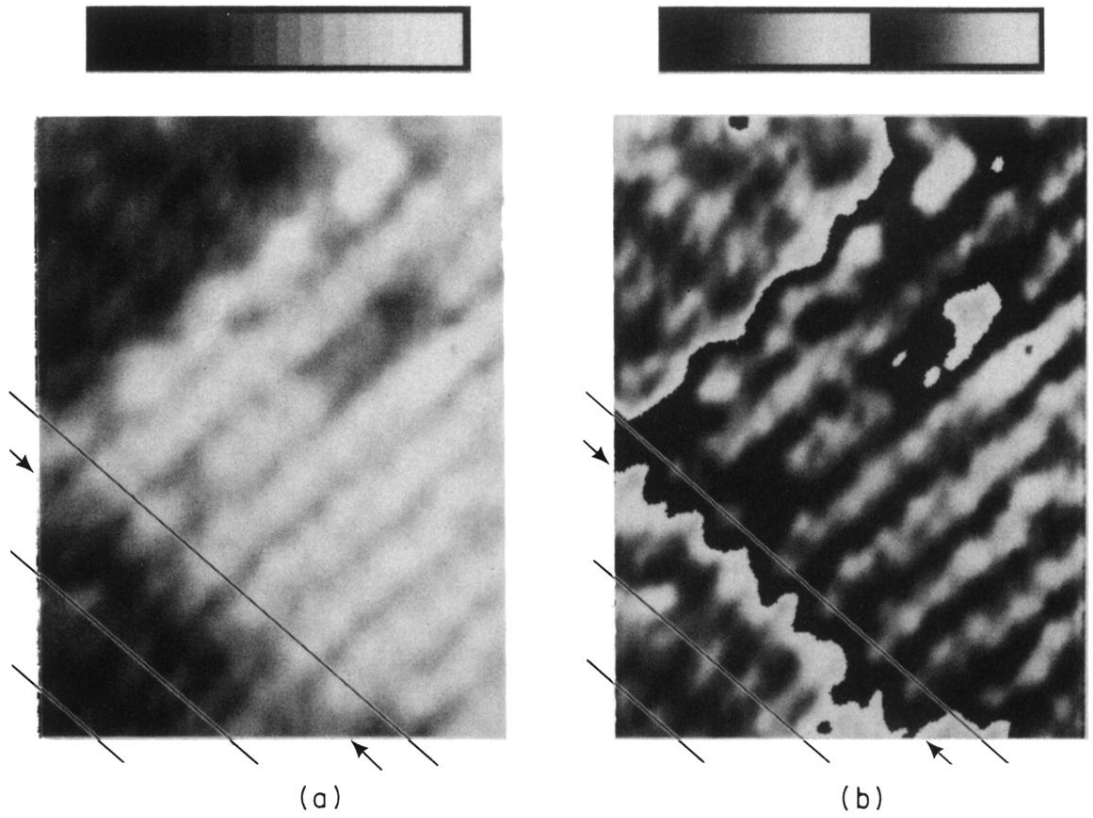

FIG. 13. Monatomic step along $\langle 1\bar{1}0 \rangle$ in which atoms forming the lower step edge participate in dimer bonding (first configuration of Fig. 12). (a) uses a single linear gray scale; the gray half-row predicted by the ACS calculations is visible. (b) are the same data imaged with a split gray scale to show the atomic spacings. Lines indicate positions of dimer rows on lower terrace and first set of dimers on upper terrace; arrows indicate position of $\langle 1\bar{1}0 \rangle$ step edge. Also note the $\langle 110 \rangle$ step edge and the large buckling at the top of this step edge, as described previously.

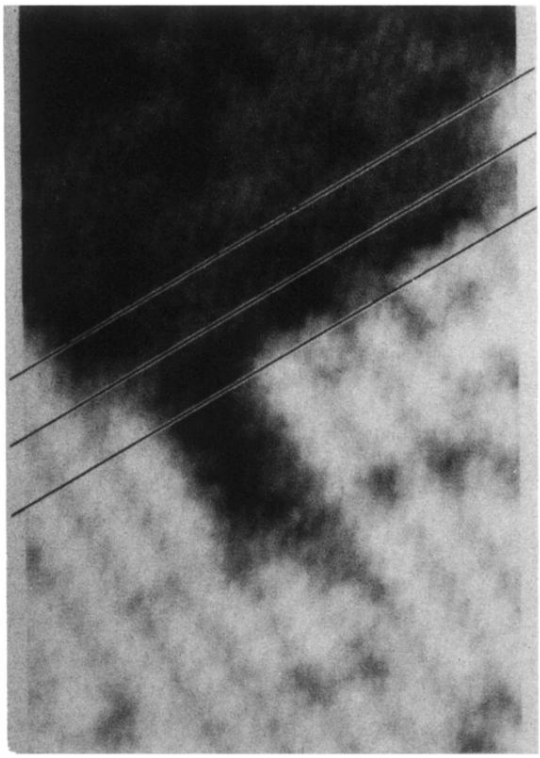

FIG. 14. Monatomic step along ⟨110⟩ in which atoms forming the lower step edge do not participate in dimer bonding (second configuration of Fig. 12).

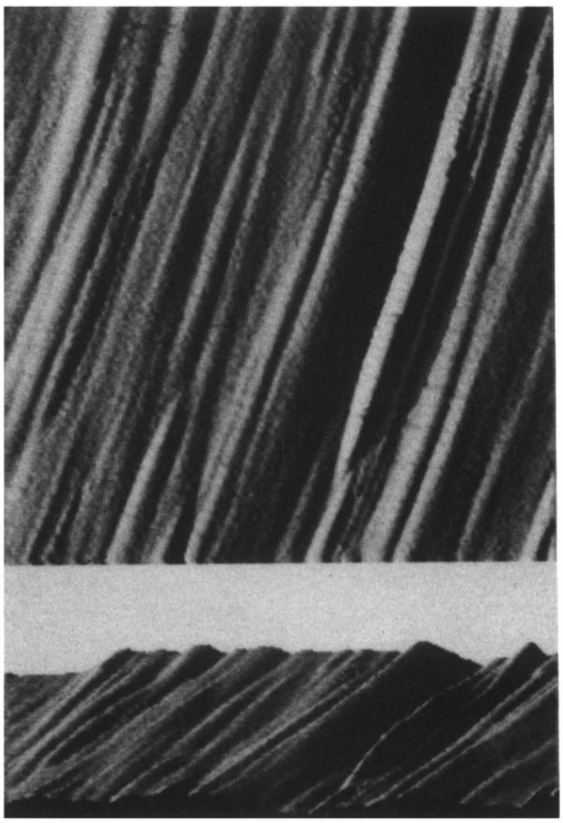

FIG. 15. 450×450 Å region of Si(001) surface which has been annealed to 1375 K and shows increased step density and initial stages of faceting. The total height variation is 14 Å. The upper image (a) is a side-illuminated topview, and the lower image (b) is a perspective view.

FIG. 16. Gray-scale image of a Si(001) surface which has been annealed to 1450 K and shows faceting. The facets appear as alternating bands at 45° with respect to the axes. The total gray-scale range is 75 Å over the 1000×1000 Å area.

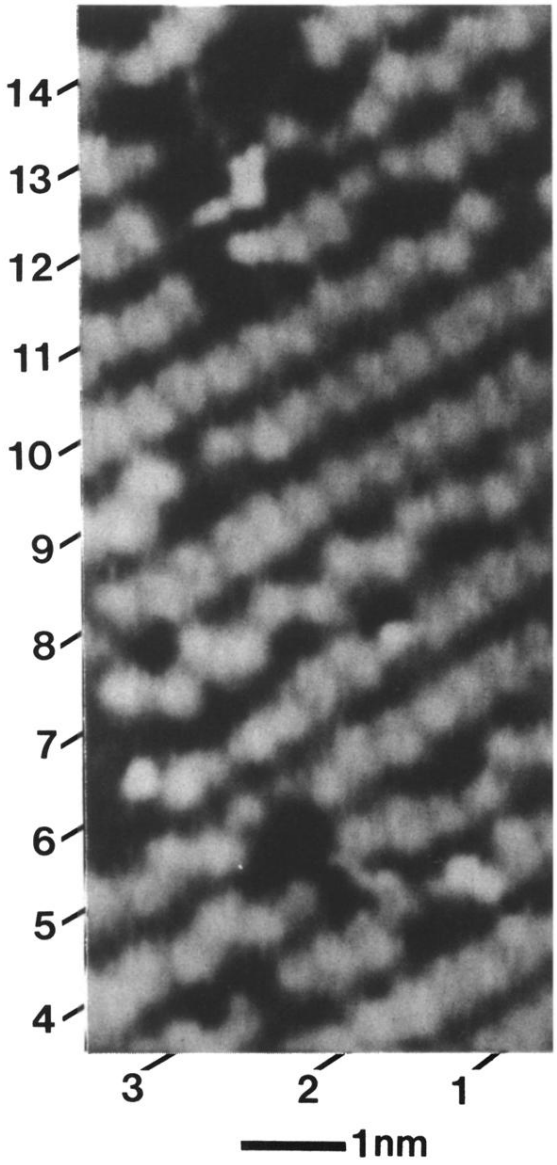

FIG. 2. Same as Fig. 1.

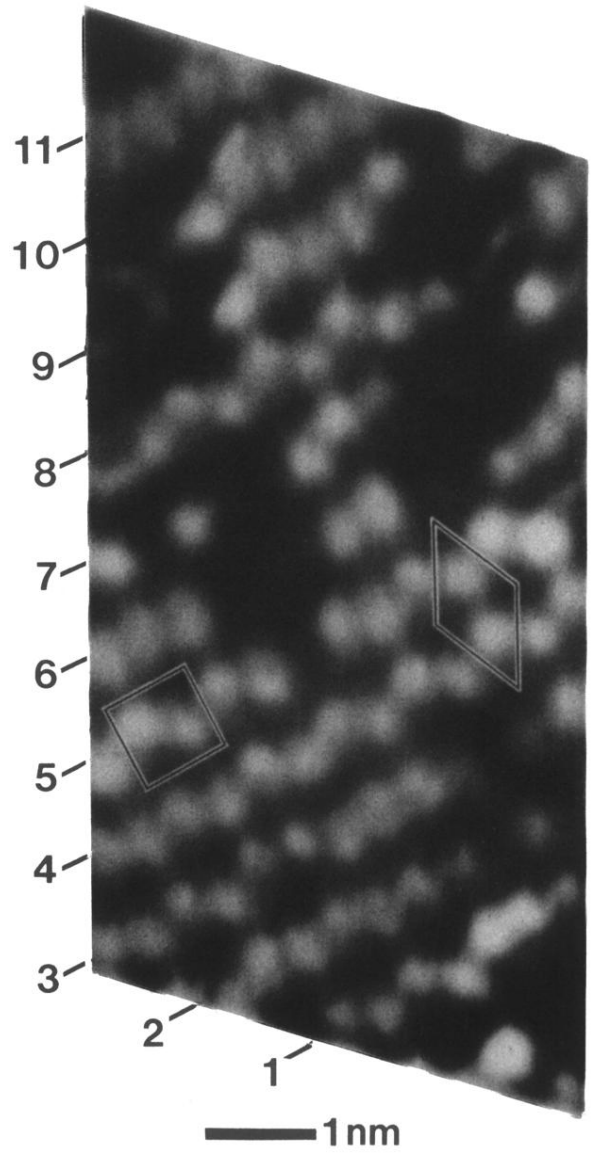

FIG. 3. Same as Fig. 1.

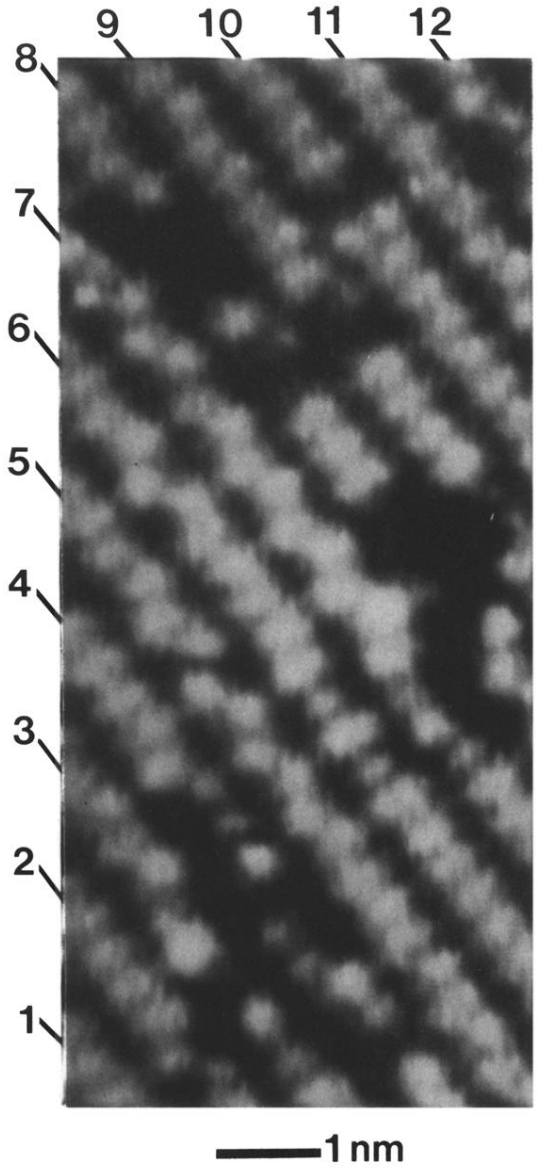

FIG. 4. Same as Fig. 1.

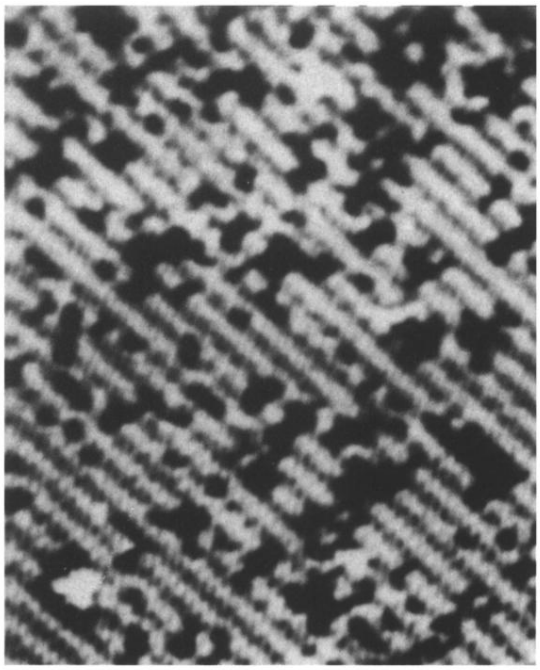

FIG. 5. Large-area topograph of the Si(001) surface illustrating the high density of vacancy-type defects. The gray scale corresponds to a distance change of 1.0 Å.

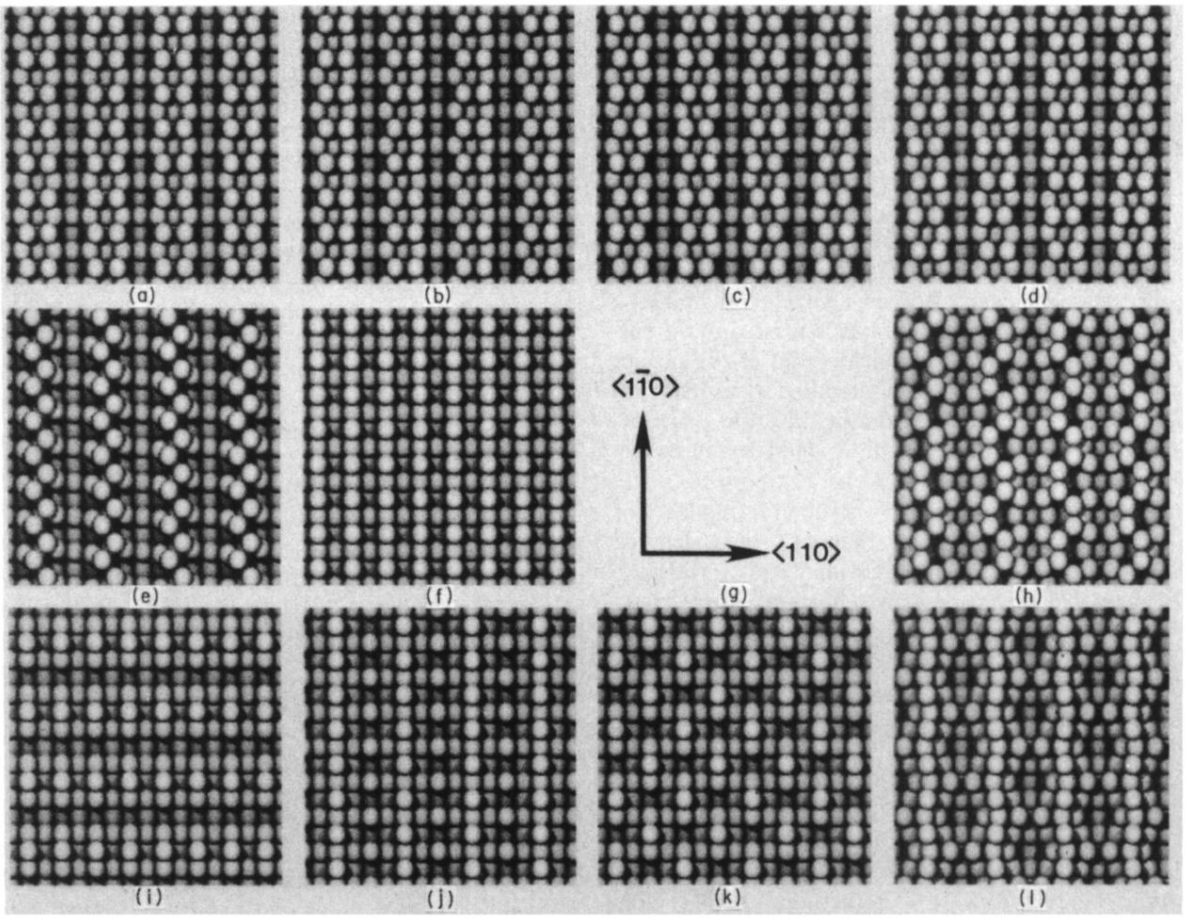

FIG. 6. Ball models of Si(001) structural models: (a) Symmetric dimer model; (b) buckled dimer models in (2×1) (c) $c(4\times2)$, and (d) $p(2\times2)$ symmetries; (e) Jona's chain model; (f) ideal (2×1) surface; (h) Northrup's dimer-plus-chain model; (i) Harrison's simple ridge, (j) symmetric ridge, and (k) $c(2\times2)$ models; (l) Poppendieck, Ngoc, and Webb's vacancy model.

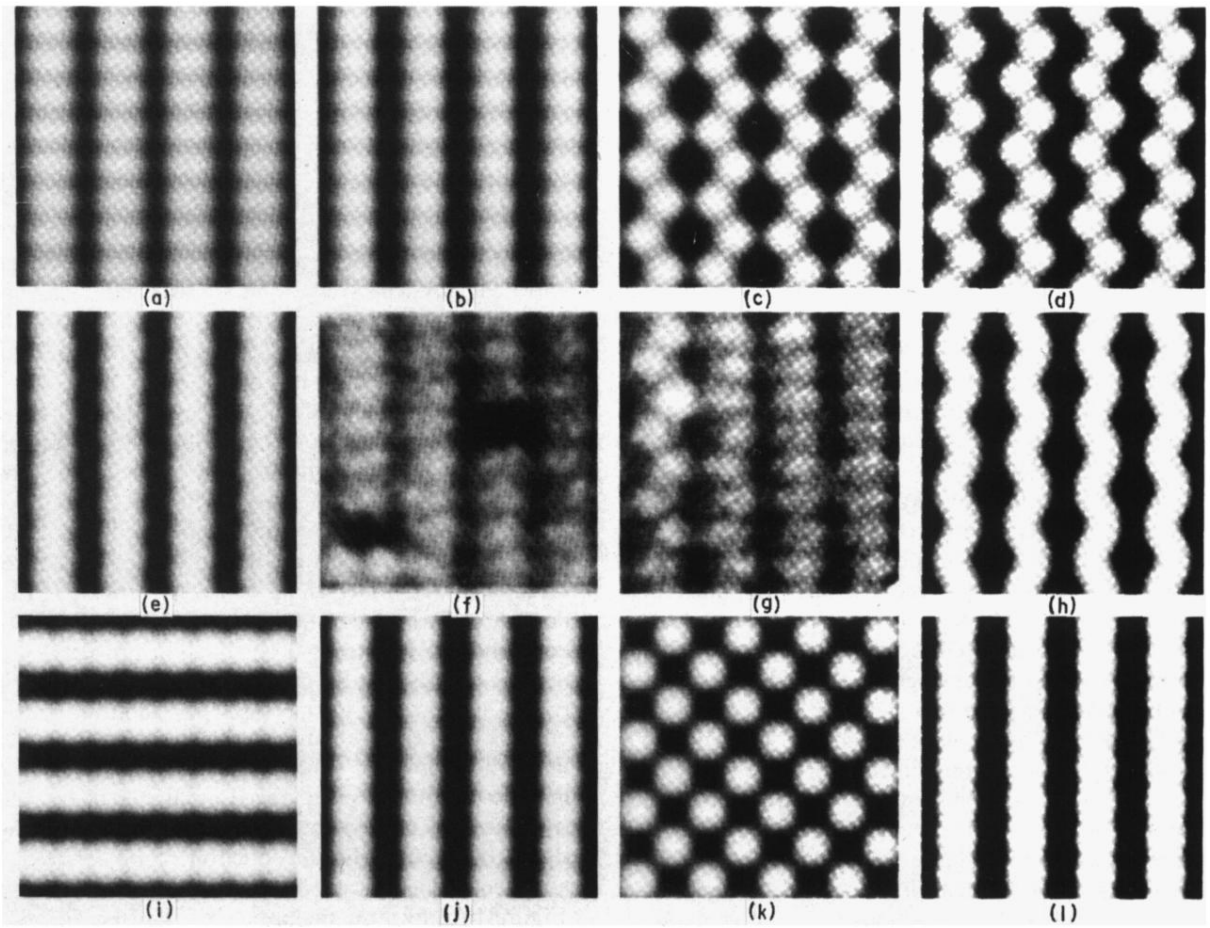

FIG. 7. Surfaces of constant charge density at 10^{-5} $e/\text{Å}^3$ for various structural models compared with experimental results: (a) Symmetric dimer model; (b) buckled dimer models in (2×1), (c) $c(4\times2)$, and (d) $p(2\times2)$ symmetries; (e) Jona's chain model; (f) experimental images from defect-free and (g) near defected regions; (h) Northrup's dimer-plus-chain model; (i) Harrison's simple ridge, (j) symmetric ridge, and (k) $c(2\times2)$ models; (l) Poppendieck, Ngoc, and Webb's vacancy model.